Multiscale Multiphysics Material Modelling

von der Fakultät Maschinenbau
der Technischen Universität Dortmund
zur Erlangung des akademischen Grades

Doktor-Ingenieur habilitatus
(Dr.-Ing. habil.)

genehmigte Habilitationsschrift

von

Dr.-Ing. Tobias Kaiser

aus Castrop-Rauxel

Kommissionsvorsitz:	Prof. Dr.-Ing. habil. A. Menzel
Referenten:	Prof. Dr. habil. S. Forest
	Prof. Dr.-Ing. D. M. Kochmann
Tag der Einreichung:	10.05.2023
Tag des Habilitationsvortrags:	08.11.2023

Bibliografische Information Der Deutschen Bibliothek
Die Deutsche Bibliothek verzeichnet diese Publikation in der Deutschen Nationalbibliografie; detaillierte bibliografische Daten sind im Internet über **http://dnb.ddb.de** abrufbar.

Bibliographic information published by Die Deutsche Bibliothek
Die Deutsche Bibliothek lists this publication in the Deutsche Nationalbibliografie; detailed bibliographic data is available in the Internet at **http://dnb.ddb.de**.

Schriftenreihe des Instituts für Mechanik

Herausgeber: Institut für Mechanik
Fakultät Maschinenbau
Technische Universität Dortmund
Leonhard-Euler-Str. 5
D-44227 Dortmund

Druck: Koffler DruckManagement GmbH

Als Manuskript gedruckt. Printed in Germany.

ISSN 2191-0022
ISBN 978-3-947323-46-3

"The capacity to learn is a gift;
The ability to learn is a skill;
The willingness to learn is a choice."

Brian Herbert, House Harkonnen

Preface

The research presented in this contribution was conducted at the Institute of Mechanics at TU Dortmund University, the Centre des Matériaux at MINES ParisTech and the Mechanics of Materials Group at Eindhoven University of Technology from spring 2019 to fall 2022. It was supported by the German Research Foundation (DFG) via the Collaborative Research Centre/Transregio 188 (Project-ID 278868966) and would not have been possible without contributions from colleagues affiliated (at that time) with the Austrian Academy of Sciences, the Karlsruhe Institute of Technology, the Max Planck Institute for Iron Research, and the University of Siegen.

Acknowledgements

Over the past years, I have been most privileged to learn from and with brilliant, open-minded colleagues and to work with them on fundamental research questions in the area of computational mechanics and materials science. First and foremost, I would like to thank my mentors Prof. Andreas Menzel (TU Dortmund University), Prof. Samuel Forest (MINES ParisTECH) as well as Prof. Marc G. D. Geers and Assoc. Prof. Joris J. C. Remmers (Eindhoven University of Technology) for their trust, encouragement and guidance. Moreover, I'm deeply indebted to my colleagues from mathematics, Prof. Thorsten Raasch (University of Siegen), and from materials science, Prof. Christoph Kirchlechner (Karlsruhe Institute of Technology), Dr. Megan J. Cordill (Austrian Academy of Sciences) as well as Prof. Gerhard Dehm and Dr. Hanna Bishara (Max Planck Institute for Iron Research). The interdisciplinary exchange of ideas that we had over the last couple of years significantly contributed to this work.

I also would like to thank Dr. Knut A. Meyer (TU Braunschweig), the team of the Collaborative Research Centre/Transregio 188 and my colleagues at the Institute of Mechanics at TU Dortmund University for many inspiring discussions. In particular, I am grateful to be able to explore and to push the limits of continuum mechanics together with M.Sc. Carina Witt, M.Sc. Dilek Güzel and M.Sc. Lennart Sobisch.

Finally, I would like to thank my wife Miriam, my family and my friends for their unconditional support.

Dortmund, November 2023 Tobias Kaiser

Zusammenfassung

Die vorliegende Arbeit befasst sich mit der skalenübergreifenden Modellierung von Materialien und ist in fünf Abschnitte gegliedert. Der erste Abschnitt beschäftigt sich mit der Entwicklung von *computergestützten Mehrskalenansätzen für elektro-mechanisch gekoppelte Probleme* elektrisch leitfähiger Materialien bei infinitesimalen und finiten Deformationen. Die Anwendbarkeit dieser Verfahren wird im zweiten Abschnitt unter Berücksichtigung *experimenteller Ergebnisse* untersucht. Angesichts der Komplexität realer Mikrostrukturen liegt der Schwerpunkt im dritten Abschnitt auf der Entwicklung einer *Grenzschichtformulierung*, um den Einfluss von materiellen Grenzflächen und von Versagensprozessen in diesen auf die effektiven elektrischen Eigenschaften der betrachteten Mikrostruktur in Simulationen abbilden zu können. Die signifikanten Rechenzeit- und Speicheranforderungen, die insbesondere bei Mehrskalenmethoden für gekoppelte Probleme vorliegen, motivieren die Behandlung effizienter Lösungsverfahren unter besonderer Berücksichtigung *wavelet- und FFT-basierter Ansätze* im vierten Abschnitt der vorliegenden Arbeit. Im abschließenden fünften Abschnitt wird die *Spannungs-Gradienten-Theorie* als alternativer Ansatz zur Berücksichtigung mikrostruktureller Eigenschaften in makroskopischen Simulationen betrachtet, wobei insbesondere der Einfluss von spannungsfreien Randschichten und damit verbundene Größeneffekte untersucht werden.

Abstract

This contribution focuses on the modelling of materials across multiple length scales and consists of five primary parts. The first part is concerned with the development of *electro-mechanically coupled computational multiscale formulations* for electrical conductors in small and finite deformation settings. Their applicability is demonstrated in the second part by a detailed comparison with *experimental findings*. Given the complexity of real microstructures, focus in the third part is laid on the development of a *cohesive zone formulation* for electrical conductors so as to account for the action of material interfaces and associated failure processes at the microscale. Addressing the severe computational effort of multiscale approaches, fast and efficient solution approaches to microscale boundary value problems are investigated and a *hybrid wavelet-FFT approach* is proposed in part four. Finally, the *stress gradient continuum theory* as an alternative approach to account for the underlying material microstructure in macroscopic simulations is discussed in part five with particular focus lying on the simulation of boundary-layer- and associated smaller-is-softer-type size effects.

Publications

The extended summary of research findings presented in this contribution is based on the following peer-reviewed journal articles:

Paper 1: T. Kaiser and A. Menzel. An electro-mechanically coupled computational multiscale formulation for electrical conductors. *Archive of Applied Mechanics*, 91: 1509–1526, 2021, [42].

Paper 2: T. Kaiser and A. Menzel. A finite deformation electro-mechanically coupled computational multiscale formulation for electrical conductors. *Acta Mechanica*, 232(10): 3939–3956, 2021, [43].

Paper 3: T. Kaiser, G. Dehm, C. Kirchlechner, A. Menzel and H. Bishara. Probing porosity in metals by electrical conductivity: Nanoscale experiments and multiscale simulations. *European Journal of Mechanics A/Solids*, 97, 104777, 2023, [46].

Paper 4: T. Kaiser, M. J. Cordill, C. Kirchlechner and A. Menzel. Electrical and mechanical behaviour of metal thin films with deformation-induced cracks predicted by computational homogenisation. *International Journal of Fracture*, 231(2): 233–242, 2021, [41].

Paper 5: T. Kaiser and A. Menzel. Fundamentals of electro-mechanically coupled cohesive zone formulations for electrical conductors. *Computational Mechanics*, 68: 51–67, 2021, [40].

Paper 6: T. Kaiser, J. J. C. Remmers and M. G. D. Geers. An adaptive wavelet-based collocation method for solving multiscale problems in continuum mechanics. *Computational Mechanics*, 70: 1335–1357, 2022, [45].

Paper 7: T. Kaiser, T. Raasch, J. J. C. Remmers and M. G. D. Geers. A wavelet-enhanced adaptive hierarchical FFT-based approach for the efficient solution of microscale boundary value problems. *Computer Methods in Applied Mechanics and Engineering*, 409, 115959, 2023, [47].

Paper 8: T. Kaiser, S. Forest and A. Menzel. A finite element implementation of the stress gradient theory. *Meccanica*, 56(5): 1109–1128, 2021, [44].

The author of this work contributed fundamental aspects with regard to the outline of the theory, carried out the numerical implementations, evaluated the simulations, and prepared the drafts of the manuscripts that were published in collaboration with one or more co-authors.

Contents

1 Introduction

This chapter provides an overview of experimental observations at various length scales and briefly discusses, in a broader sense, modelling approaches that are taken to account for these in numerical simulations. In particular, the experimental observations and numerical approaches summarised in Section 1.1 motivate the research questions that are formulated in Section 1.2 and that build the basis for the present contribution.

1.1 Motivation and state of the art

After a brief introduction to (multiscale) material modelling in Section 1.1.1, fundamental observations with regard to conducting materials are highlighted in Section 1.1.2 before the focus is laid on wavelet-based approaches in Section 1.1.3 and on generalised continuum approaches in Section 1.1.4.

1.1.1 Materials with microstructure

Computational mechanics is a considerably interdisciplinary discipline integrating, amongst others, knowledge and methods from materials science, scientific computing and manu-

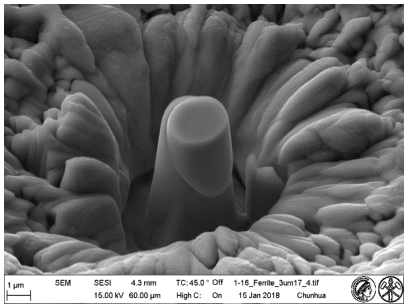

(a) microscale experiment (courtesy of C. Kirchlechner, Karlsruhe Institute of Technology)

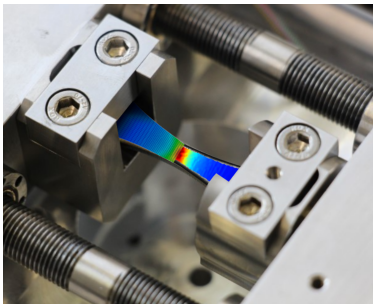

(b) macroscale simulation (courtesy of L. Rose, TU Dortmund University)

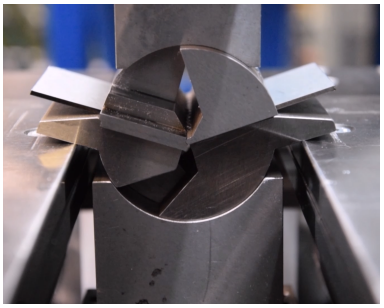

(c) macroscale forming process (courtesy of A. E. Tekkaya and R. Meya, TU Dortmund University)

Figure 1.1: On experimental investigations at multiple scales, the development of simulation-based approaches and the application to forming processes: a) Micropillar compression test to determine the critical resolved shear stress of ferrite in DP800 steel. b) Comparison of finite element-based macroscale simulation results with experimental data obtained by using digital image correlation. c) Radial stress superposed bending (RSS bending) of DP800 sheet material.

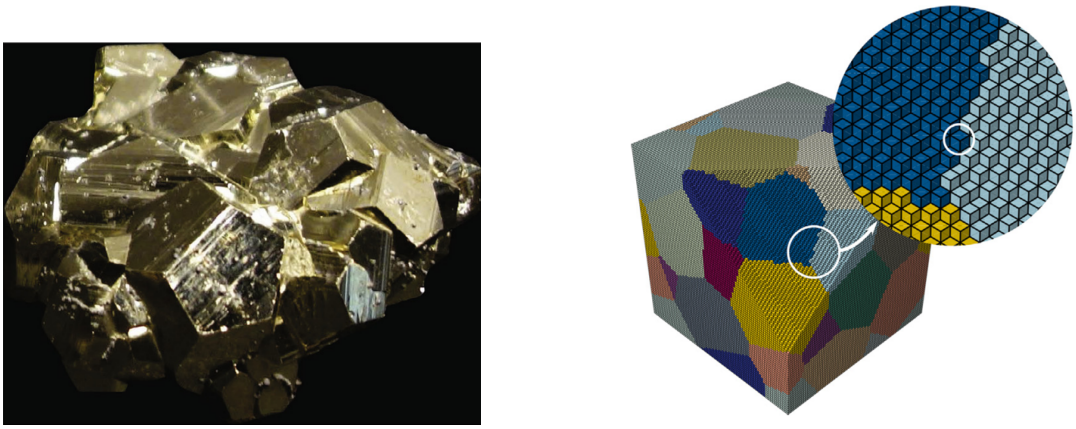

(a) pyrite (Fe_2S) (b) voxel-based discretisation

Figure 1.2: Polycrystalline pyrite (Fe_2S) and voxel-based discretisation of a representative volume element for a polycrystalline solid. Reproduced from [9] under the terms of the Creative Commons Attribution-NonCommercial-No Derivatives License (CC BY NC ND).

facturing technologies with the ultimate goal of predicting material behaviour. Today, experimental findings at various length scales build the basis for the development of state of the art material models. This is exemplified in Figure 1.1 where experimental investigations at the micro- and macroscale, finite element-based macroscale simulation results and a forming process at the macroscale are shown. Without any doubt, the underlying microstructure and the physical processes taking place at the microscale determine the effective material response at the macroscale, for which a thermodynamically consistent mathematical description in terms of material models is required to simulate the forming process.

As opposed to classic phenomenological material models that postulate constitutive relations based on the experimentally observed effective material behaviour at the macroscale, computational multiscale methods allow detailed information of the microstructure and micromechanics models that have been developed at the level of individual phases to be accounted for. To this end, the underlying microstructure is geometrically resolved in so-called representative volume elements as exemplarily shown in Figure 1.2, see also [9, 23, 89], and the evaluation of macroscale material models is substituted by detailed microstructure simulations. By introducing scale-bridging relations, quantities at the different scales under consideration are related to each other. In particular, macroscale fields are defined as volume averages of their microscopic analogues, boundary conditions for the microscale boundary value problem are determined by macroscopic fields, and energetic consistency conditions are established.

Originating from the pioneering works [82, 94] computational multiscale methods are meanwhile well-established in the computational mechanics community, see [26, 27, 61, 87] for detailed reviews. For purely mechanical problems, first-order computational

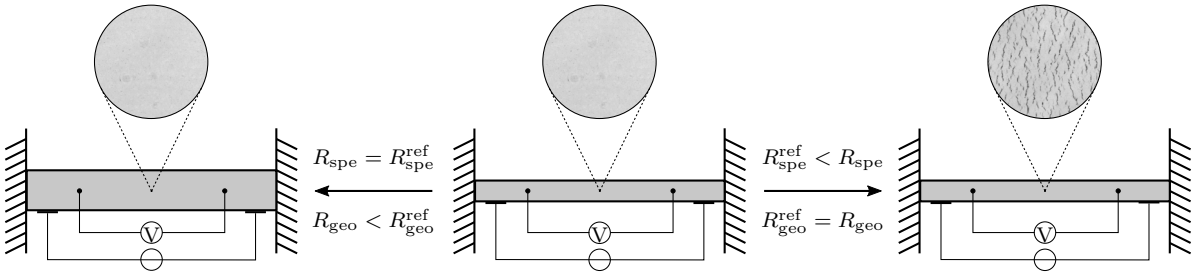

Figure 1.3: Differences in the geometric dimensions and in the underlying microstructures of the idealised wire-like structures (left, right) manifest themselves in different geometric and specific resistances compared to the reference specimen (middle). Reproduced from [42] under the terms of the Creative Commons Attribution 4.0 International License (CC BY 4.0).

homogenisation schemes are for instance discussed in [14, 15, 53, 63–66]. The extension to generalised continuum theories by additionally taking the second gradient of the placement field into account has been studied in, e.g., [35, 54, 55, 76]. Moreover, computational homogenisation schemes for thermo-mechanically coupled problems are addressed in [10, 11, 80, 90, 95], formulations for magneto-mechanically coupled problems are discussed in [36, 93], and formulations that focus on the simulation of piezo- and ferroelectric materials are elaborated in [48, 49, 88]. In contrast to the theoretical developments on (dielectric) electro-active solids discussed in [48, 49, 88], a particular focus of the present contribution lies on the development of electro-mechanically coupled computational multiscale formulations for electrical conductors as motivated by the experimental observations discussed in Section 1.1.2.

1.1.2 Electro-mechanical coupling

For motivation purposes, assume for now a homogeneous, quasi-one-dimensional electrical toy problem for which the effective macroscopic electrical resistance is given by

$$R = \frac{1}{\kappa}\,\frac{L}{A} = R_{\mathrm{spe}}\,R_{\mathrm{geo}}\,, \quad R_{\mathrm{spe}} = \frac{1}{\kappa}\,, \quad R_{\mathrm{geo}} = \frac{L}{A} \quad . \tag{1.1}$$

While the geometrical contribution R_{geo} to the electrical resistance is defined by the macroscopic length L and cross-sectional area A of the conductor, the specific resistance R_{spe} which is defined as the inverse conductivity κ is an effective macroscopic material parameter that accounts for the (possibly inhomogeneous) material microstructure. The different contributions to the effective macroscopic resistance are exemplified in Figure 1.3 for a material featuring microstructural imperfections.

Gaining a detailed understanding and predicting the influence of microscale features such as the phase composition, grain- and phase boundaries or micro-cracks on the effective electrical conductivity is of importance for manufacturing technologies and reliability engineering alike:

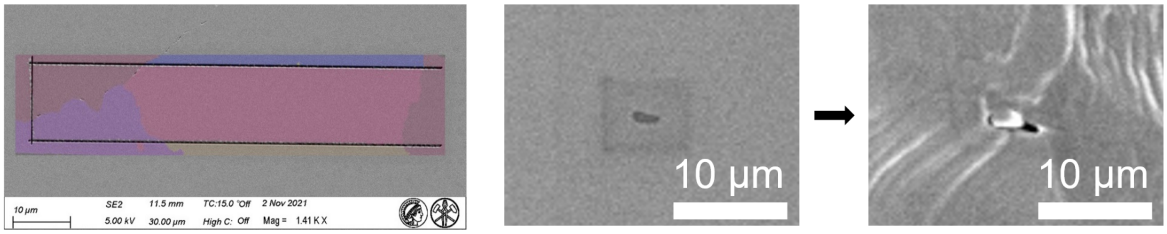

(a) grain boundary resistivity in Cu films (courtesy of H. Bishara, MPIE)

(b) MnS-delamination and void growth in 16 $MnCrS_5$ (courtesy of A. Dunlap, RWTH Aachen)

Figure 1.4: Exemplary studies of grain and phase boundaries in the context of electrical conductivity and deformation-induced failure processes: a) Electron backscatter diffraction-based analysis of grain orientations in a Cu thin film sample, used in a study of grain boundary resistivity. b) Experimental analysis of damage evolution in the vicinity of MnS inclusions in 16 $MnCrS_5$ steel using scanning electron microscopy.

Firstly, consider as an example flexible electronic devices such as wearable sensors [5, 69] and foldable displays [12, 51], which are in the focus of many engineering applications. To ensure the functionality of these devices, detailed knowledge is required on the electro-mechanical material properties for various loading conditions. However, the experimental characterisation of material thin films, especially the study of failure mechanisms, is difficult and requires the development of advanced measuring technologies as discussed in [16, 28, 58]. Computational multiscale homogenisation schemes are promising numerical approaches to support these developments as they allow material microstructures and their evolutions to be resolved in numerical simulations. Moreover, complex deformation processes which are difficult to study experimentally are accessible by using suitable computational multiscale formulations that were calibrated on the basis of experiments and enable predictive simulations.

Secondly, experimentally recorded electrical signals at the macroscale may be interpreted as a fingerprint of the material state. Against this background, computational multiscale formulations for conductors are expected to contribute to the development process of advanced non-destructive electrical resistance-based testing methods used to analyse defect structures in specimens, e.g., [52].

Focusing in more detail on the microscale, the electrical characterisation of individual grain boundaries in a Cu film is exemplarily shown in Figure 1.4(a) and the experimentally observed delamination process of a MnS particle in 16 $MnCrS_5$ steel is shown in Figure 1.4(b). As opposed to the bulk properties of individual microscale phases, both experimental investigations are intrinsically related to material interfaces. The former study is concerned with the additional resistivity measured due to the presence of grain boundaries, the latter with the evolution of interface damage and void growth at the microscale that is, likewise, expected to affect the effective conductivity. The distinct properties of the interfaces in the previous examples differ significantly from those of the surrounding continuum and can be accounted for in simulations by the introduction of

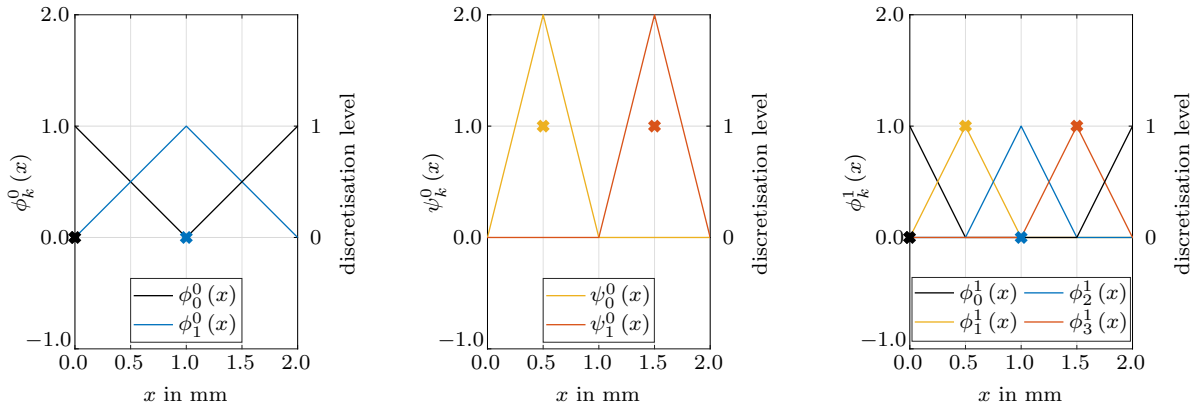

(a) level 0 scaling functions (b) level 0 wavelets (c) level 1 scaling functions

Figure 1.5: Hat-wavelets and scaling functions on a periodic domain with period 2.0 mm. The domain is discretised with two grid points on discretisation level 0 and four grid points are used in the corresponding level 1 discretisation. Crosses indicate the spatial positions and the discretisation levels on which grid points occur for the first time. It is observed that the grid point at $x = 0.0\,\text{mm}$ is associated with scaling function ϕ_0^0 in a level 0 discretisation and with scaling function ϕ_0^1 in a level 1 discretisation. Likewise, the grid point at $x = 0.5\,\text{mm}$ is associated with wavelet ψ_0^0 and scaling function ϕ_1^1, respectively. Reproduced from [45] under the terms of the Creative Commons Attribution 4.0 International License (CC BY 4.0).

interface models. In these approaches, the physical interface (of finite thickness) is not geometrically resolved but rather approximated as a lower-dimensional object (e.g. as a surface in a three-dimensional setting).

Based on the assumed continuity of field quantities across the interface, different types of interface formulations may be distinguished, see [37] and references cited therein. Elastic-interface models originate from the pioneering works of Gurtin and Murdoch on interface elasticity [30, 74], and assume the displacement-type fields to be continuous, whereas traction-type quantities may exhibit jump-discontinuities across the interface. Classic cohesive interface models that date back to the seminal works by Barenblatt on quasi-brittle materials [8] and by Dugdale on ductile materials [19] on the other hand, assume traction continuity across the interface and allow for the modelling of jump-discontinuities in the displacement-type fields. Although seemingly different, it has recently been shown that classic cohesive zone formulations and interface elasticity formulations can be regarded as two extremes of the unifying theory of generalised imperfect interfaces elaborated in [37, 38, 79, 85].

Since the works of Barenblatt and Dugdale [8, 19], classic cohesive zone models that are in the focus of the present contribution have been subject of intense research with many contributions focusing on the consistency of cohesive zone formulations with fundamental requirements of continuum mechanics (particularly for finite deformations), e.g. [71, 78, 99, 105], and on the elaboration of specific traction separation laws that account for irreversible processes such as damage and plasticity, e.g. [20, 33, 77, 83, 98, 107]. In

addition to the developments on cohesive zone formulations for purely mechanical problems, cohesive zone formulations for coupled multi-physics problems have been studied. In particular, thermo-mechanical coupling has been addressed in [21, 22, 81] and electro-mechanically coupled cohesive zone formulations for electro-active solids have been proposed in [4, 56, 57, 97, 103, 104]. However, focussing on piezo- and ferroelectric effects in dielectric solids, the latter formulations differ significantly from the developments on electrical conductors in the present contribution.

The experimental results summarised in this section show that computational multiscale methods intrinsically rely on an accurate representation of the underlying microstructure, both in terms of its morphology and the constitutive response of individual constituents. For this reason, the repetitive solution of microscale boundary value problems is associated with significant computational costs and memory requirements, in particular in multi-physics applications or when non-linear constitutive relations are to be solved [26]. Against this background, elaborated numerical approaches for the efficient solution of microscale boundary value problems are discussed in Section 1.1.3

1.1.3 Wavelet-based approaches

Wavelet analysis emerged in the early 1980s, driven by applications in seismic geology [70], electrical engineering [92] and quantum science [29]. It is based on the fundamental concept of multiresolution analysis [60] and has been shown to be particularly useful in the study of physics problems that include characteristic features at significantly different length scales. Hence, it is often also referred to as the numerical microscope [59]. By providing an hierarchical sequence of basis functions and by establishing transformation relations between the different resolution levels considered, wavelet-based approaches allow signals to be systematically analysed and compressed by successively "peeling off" high frequency components. Vice versa, compressed signals may be retrieved and detailed representations of a signal may be derived by making use of wavelet synthesis operations. In this regard, wavelet-based approaches differ significantly from classic spectral approaches since wavelet basis functions have good localisation properties in both physical and spectral space. This eventually allows the determination of the frequency spectrum of a signal and the locations in physical space at which particular frequencies occur [106], and to properly resolve localised features of a signal by systematically adding/removing higher level wavelets in the respective wavelet expansion.

As an example, consider the wavelet family depicted in Figure 1.5. By adding level 0 wavelets $\psi_k^0(x)$ (spanning the wavelet space $\mathcal{W}^0$) to level 0 scaling functions (spanning the scaling function space $\mathcal{V}^0$) one arrives at a level 1 discretisation space ($\mathcal{V}^1 = \mathcal{V}^0 \oplus \mathcal{W}^0$). In addition to the intrinsically hierarchical character, the previous example demonstrates an interesting characteristic of classic wavelet-based approaches: scaling functions and wavelets at the different resolution levels are translates and dilates of mother scaling functions and mother wavelets, respectively.

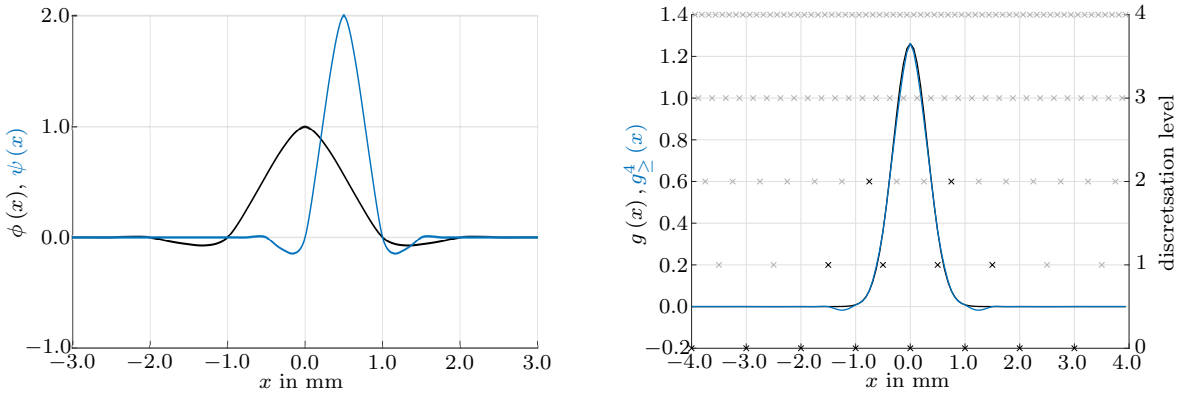

(a) scaling function and wavelet

(b) wavelet expansion of Gaussian

Figure 1.6: Exemplary wavelet expansion in a one dimensional setting using Deslauriers-Dubuc wavelets: a) Deslauriers-Dubuc scaling function and wavelet ($N = 2$). b) One-dimensional periodised Gaussian $g(x) = [0.2 * \pi]^{-0.5} \exp\left(-5x^2\right)$ with period 8 and level 4 wavelet expansion $g_{\geq}^{4}(x)$ using Deslauriers-Dubuc wavelets ($N = 2$). Active grid points are indicated in black colour, inactive grid points in grey colour. Reproduced from [47] under the terms of the Creative Commons Attribution-NonCommercial-NoDerivatives 4.0 International License (CC BY-NC-ND 4.0).

Focusing on wavelet-based representations of functions, the approximation of a Gaussian in a one-dimensional setting is shown in Figure 1.6 where wavelet-coefficients smaller than tolerance ϵ_d where neglected in the general wavelet expansion

$$f(x) \approx f_{\geq}^{j}(x) = \sum_{k} s_k^0 \, \phi_k^0(x) + \sum_{i=0}^{j-1} \sum_{\substack{k \\ |d_k^i| \geq \epsilon_d}} d_k^i \, \psi_k^i(x) \quad . \tag{1.2}$$

In (1.2), $f(x)$ denotes a scalar-valued function that is approximated at different resolution levels j in terms of scaling function coefficients s_k^j and wavelet coefficients d_k^j, with index k indicating translation in space. In addition to the one-dimensional example shown in Figure 1.6, the wavelet-based representation of a two-dimensional field – a greyscale image of the mechanical engineering building at TU Dortmund University – is shown in Figure 1.7. Whereas almost all information is lost when naively compressing the image by taking only information of pixels in the top left corner into account, important information such as the reference to the Institute of Mechanics or the address and building number are still recognisable in the wavelet-compressed image. This example demonstrates that the complexity of problems (in this case the number of greyscale values stored) can significantly be reduced while preserving most of the information by using adaptive hierarchical wavelet approaches.

Due to their remarkable time-frequency decomposition characteristics, adaptive wavelet-based approaches to the solution of (partial) differential equations have been in the

(a) original 2048×1024 pixel image

(b) 90% compressed image relying only on information of the top-left corner

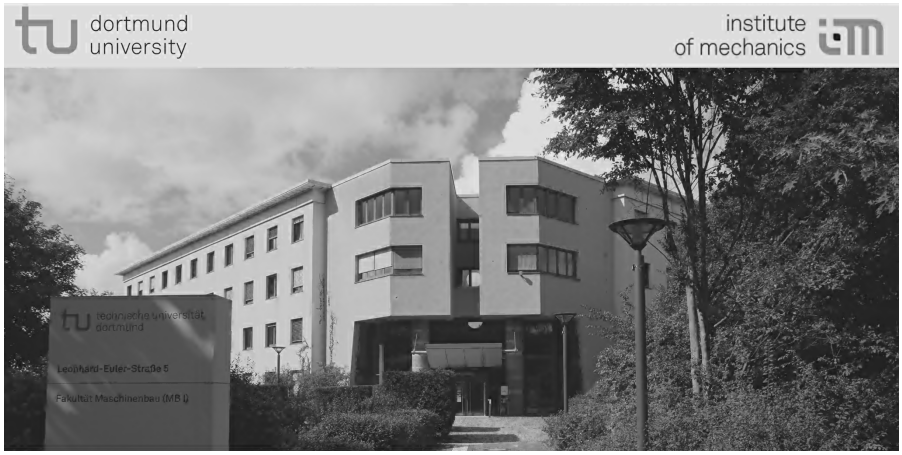

(c) 90% compressed image based on wavelet analysis

Figure 1.7: On targeted refinement and the representation of information: a) Original 2048×1024 pixel image. b) Naive image compression by taking only information of pixels in the top-left corner into account. c) Image compression by using Deslauriers-Dubuc wavelets ($N = 2$, three discretisation levels) and by dropping "small" wavelet coefficients in the wavelet-expansion.

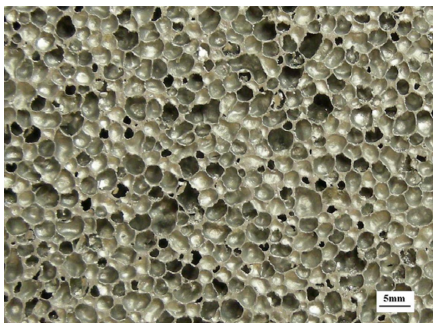

(a) closed-cell aluminium foam (reprinted from [91], copyright (2010), with permission from Elsevier)

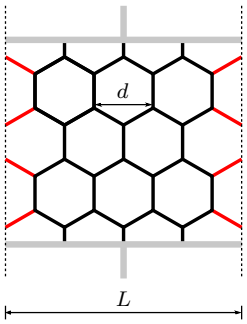

(b) compression test (motivated by [75])

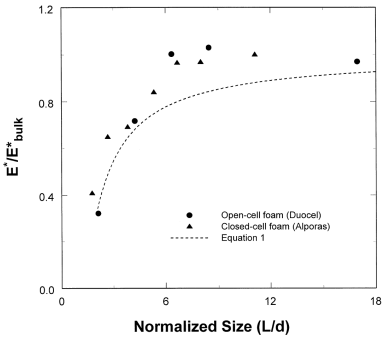

(c) experimentally observed size effect (reprinted from [3], copyright (2001), with permission from Elsevier)

Figure 1.8: Boundary layer and size effects in closed-cell aluminium foams. a) Microstructure of a closed-cell aluminium foam (ALPORAS©). b) Compression test of a foam-type sample of length L and with pore diameter d. c) Experimentally determined unloading stiffness E^* for different foams. The dashed line represents the solution derived in [75] based on simulations with a fully resolved microstructure.

focus of intense research, see [59] for a detailed review. These include wavelet collocation [31, 32, 102], wavelet Galerkin [1, 2, 39] and wavelet finite element methods [13]. However, applications to continuum mechanics problems have been rather limited and there are but a few works that focus for instance on the application of wavelets to structural optimisation problems [50], on wavelet-enhanced finite element-based approaches for the efficient solution of microscale boundary value problems [6, 7] or on adaptive wavelet-based reduced order models [100, 101]. Against this background, the applicability of wavelet-based approaches to reduce the computational complexity of microscale boundary value problems and the combination of these approaches with state of the art spectral solvers is studied in this contribution. Moreover, given the computational effort that is still associated with elaborate multiscale schemes, alternative approaches to account for the effect of the underlying microstructure in macroscale simulations are additionally considered in Section 1.1.4.

1.1.4 Stress gradients, boundary layer and size effects

For motivation purposes consider the closed-cell aluminium foam depicted in Figure 1.8(a) and assume that the foam is subjected to a compressive load state as schematically shown in Figure 1.8(b) for a simplified two-dimensional setting. In this example, two characteristic measures of unit length occur: 1) the (average) cell diameter d and 2) the macroscopic sample size L. Moreover, it is observed that the outer cells, marked in red colour, are stress-free and do not contribute to the overall effective stiffness which is, hence, a function of the internal length d and the sample size L. This size dependence was studied experimentally in [3] and numerically in [75], where use was made

of analytical solutions and finite element-based simulation results for beam-networks. The corresponding experimental data is provided in Figure 1.8(c) along with the predicted normalised stiffness of the samples. Both experiment and simulation results show a striking smaller-is-softer-type size effect that is explained in [3, 75] by reduced kinematic constraints in the cells close to the boundary and by an increasing area fraction of the (stress-free) boundary layer with decreasing sample size.

As a counter part to well-established strain gradient theories [67, 68], a stress-gradient continuum theory has recently been proposed in [24]. Belonging to the class of micromorphic continuum approaches, the stress gradient theory relies on the introduction of additional macroscopic degrees of freedom. These so-called micro-displacements are work-conjugate to the deviatoric part of the stress gradient and associated with the deformation of the underlying microstructure. In particular, it has been shown in [34] that, by making use of a generalised computational homogenisation approach, the micro-displacements can be interpreted as the (deviatoric part of the) first moment of the micro-strainfield. In addition to this physical motivation of stress gradient continua, the well-posedness of boundary value problems for different sets of boundary conditions has been shown in [84] and an analytical solution to Eshelby's inclusion problem for stress gradient continua was derived in [96].

In the light of the experimental investigations discussed at the beginning of this section, a salient feature of the stress gradient theory is the natural occurrence of an internal length scale that allows smaller-is-softer-type size effects to be accounted for in simulations. This is in striking contrast to smaller-is-stiffer-type size effects that are encounter in classic gradient elasticity approaches. Furthermore, it is noted that the stress gradient theory allows for the (complete) stress tensor to be controlled at the boundaries such that stress-free boundary layer effects can be taken into account.

1.2 Scope and research questions

The experimental findings and modelling approaches summarised in Section 1.1 motivate research questions that guide the developments presented in this contribution. In particular, eight research questions are formulated in the following that are directly related to the publications (**Paper 1**–**Paper 8**) this contribution is based on.

From a materials science point of view, a numerical tool is required that enables a detailed study of the influence of different microscale features and processes under different loading conditions on the effective electrical conductivity. Computational multiscale formulations are expected to provide such capabilities so that the first two research questions read

RQ 1: *Can a computational multiscale formulation for electrical conductors be developed that enables a detailed study of the influence of deformation-induced microscale processes on the effective electrical conductivity in an infinitesimal deformation setting?*

RQ 2: *Can a computational multiscale formulation for electrical conductors be developed that enables a detailed study of the influence of deformation-induced microscale processes on the effective electrical conductivity in a finite deformation setting?*

The applicability of the multiscale scheme is studied in a next step by taking into account experimental data and by addressing the research questions

RQ 3: *Can the experimentally recorded resistivity of artificially generated, geometrically well-defined microstructures be reproduced by applying the developed computational multiscale scheme?*

RQ 4: *Can the experimentally recorded changes in the electrical properties of metal thin films be related to experimentally recorded microscale cracks by accounting for CLSM laser intensity information in simplified two-dimensional representative volume elements?*

With the experimentally-validated multiscale scheme at hand, focus is laid on the modelling of different microscale features that affect the electrical conductivity as formalised in the research question

RQ 5: *Can electro-mechanical properties of material interfaces (grain boundaries, phase boundaries, cracks...) be accounted for in simulations by using multi-field cohesive zone formulations?*

To address the significant computational effort that is associated with computational multiscale approaches, efficient solution schemes that make use of the characteristic structure of the microscale boundary value problem are studied thereafter in the light of the research questions

RQ 6: *What are the key properties of wavelet-based approaches – are wavelet-based approaches promising candidates to improve the overall computational efficiency of multiscale schemes?*

RQ 7: *Can adaptive hierarchical wavelet approaches be used to (further) increase the computational efficiency of FFT-based spectral solvers for microscale boundary value problems?*

and alternative, generalised continua-based approaches to account for microscale features in macroscale simulations are finally pursued

RQ 8: *Can a finite element implementation of the stress gradient theory that allows one to account for stress-free boundary layer- and associated smaller-is-softer-type size effects be derived?*

2 Extended summary

Guided by the research questions posed in Section 1.2, an extended summary of research findings published in the peer-reviewed journal articles **Paper 1**–**Paper 8** is provided in this chapter. In particular, computational multiscale approaches for electrical conductors (**Paper 1**, **Paper 2**) and their application to experiments (**Paper 3**, **Paper 4**) are discussed in Section 2.1 and Section 2.2, respectively. Focusing on the modelling of material interfaces, the fundamentals of electro-mechanically coupled cohesive zone formulations (**Paper 5**) are studied next in Section 2.3. Thereafter, focus is laid on efficient wavelet-based solution approaches for microscale boundary value problems (**Paper 6**, **Paper 7**) in Section 2.4 before the stress gradient theory (**Paper 8**) as an alternative approach to account for the underlying material microstructure is addressed in Section 2.5.

2.1 Computational multiscale modelling of conductors

The fundamentals of computational multiscale approaches for electrical conductors in infinitesimal (**Paper 1**, Section 2.1.1) and finite (**Paper 2**, Section 2.1.2) deformation settings are summarised in this section and their applicability is demonstrated by a study of selected (academic) boundary value problems.

2.1.1 Infinitesimal deformation setting

By assuming a quasi-static, quasi-stationary setting and by neglecting body forces and temperature effects, the governing set of balance equations for electrical conductors reduces to the balance equation of linear momentum and the continuity equation for the electric charge, namely,

$$\nabla \cdot \boldsymbol{\sigma} = \mathbf{0} \quad , \qquad \text{(2.1a)} \qquad\qquad \nabla \cdot \boldsymbol{j} = 0 \quad . \qquad \text{(2.1b)}$$

The stresses $\boldsymbol{\sigma}$ and the electric current density vector $\boldsymbol{j}$ that occur in the coupled set of partial differential equations (2.1) require constitutive specification. In classic phenomenological modelling approaches, constitutive relations in terms of strains $\boldsymbol{\varepsilon}$, electric field vector $\boldsymbol{e}$, and possibly a set of internal variables are postulated in accordance with the dissipation inequality. Thereafter, the field equations are solved for the primary fields of interest – the displacement field $\boldsymbol{u}$ and the electric potential field ϕ – that are

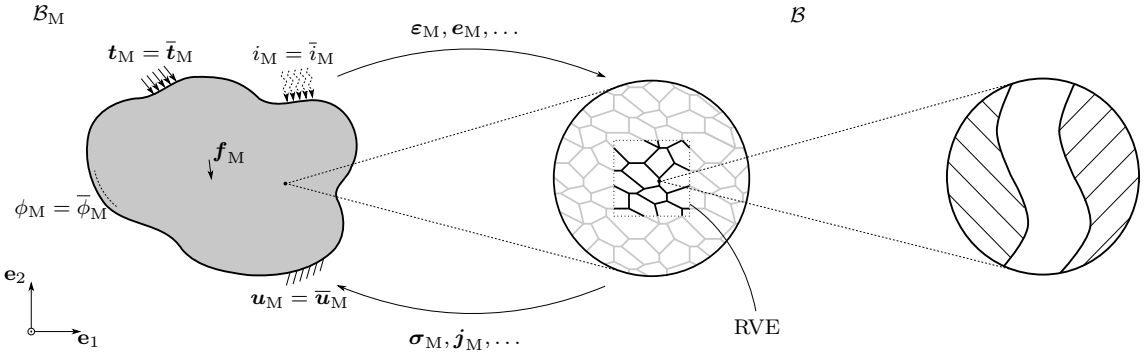

Figure 2.1: First-order computational homogenisation scheme for electro-mechanical problems. At the microscale different material regions, representing for example different grains, are indicated (middle figure). In addition, cracks that are geometrically resolved are schematically depicted (right figure). Prescribed quantities, such as tractions $\bar{\boldsymbol{t}}_\mathrm{M}$ or electric current density $\bar{i}_\mathrm{M}$, are denoted with an overbar.

related to the former kinematic quantities according to

$$\boldsymbol{\varepsilon} = \frac{1}{2}\left[\nabla \boldsymbol{u} + [\nabla \boldsymbol{u}]^\mathrm{t}\right] \quad , \qquad (2.2a) \qquad\qquad \boldsymbol{e} = -\nabla \phi \quad . \qquad (2.2b)$$

In the electro-mechanically coupled computational multiscale approach developed in **Paper 1**, the evaluation of the phenomenological macroscale material model is substituted by the solution of a microscale boundary value problem as schematically shown in Figure 2.1. To this end, an extended form of the Hill-Mandel energy equivalence condition together with the associated set of micro-macro and macro-micro scale bridging relations is established, a finite element-based implementation is derived, and representative boundary value problems are studied.

The consistent macroscale tangent stiffness tensors of the electrical problem are of particular interest for the developments in **Paper 3** and **Paper 4**. These can be extracted from the finite element discretised microscale boundary value problem and take the specific form

$$\Delta \boldsymbol{j}_\mathrm{M} \approx \underbrace{\left[\frac{1}{v}\sum_{i=1}^{\mathrm{n_{pn}}}\sum_{j=1}^{\mathrm{n_{pn}}} {}^{(i)}\boldsymbol{x} \otimes {}^{(ij)}\widehat{\mathbf{K}}^{\phi \boldsymbol{u}} \otimes {}^{(j)}\boldsymbol{x}\right]}_{= \dfrac{\mathrm{d}\boldsymbol{j}_\mathrm{M}}{\mathrm{d}\boldsymbol{\varepsilon}_\mathrm{M}}} : \Delta \boldsymbol{\varepsilon}_\mathrm{M} + \underbrace{\left[-\frac{1}{v}\sum_{i=1}^{\mathrm{n_{pn}}}\sum_{j=1}^{\mathrm{n_{pn}}} {}^{(ij)}\widehat{\mathbf{K}}^{\phi\phi}\, {}^{(i)}\boldsymbol{x} \otimes {}^{(j)}\boldsymbol{x}\right]}_{= \dfrac{\mathrm{d}\boldsymbol{j}_\mathrm{M}}{\mathrm{d}\boldsymbol{e}_\mathrm{M}}} \cdot \Delta \boldsymbol{e}_\mathrm{M} \qquad (2.3)$$

where v is the volume of the representative volume element, $\mathrm{n_{pn}}$ the number of finite element nodes where the displacement is prescribed, ${}^{(i)}\boldsymbol{x}$ the position of node i, and ${}^{(ij)}\widehat{\mathbf{K}}^{\bullet *}$ the (generalised) stiffness contribution related to nodes i and j. The contribution $\frac{\mathrm{d}\boldsymbol{j}_\mathrm{M}}{\mathrm{d}\boldsymbol{\varepsilon}_\mathrm{M}}$ is a measure for deformation-induced changes in the electrical conductivity, e.g.,

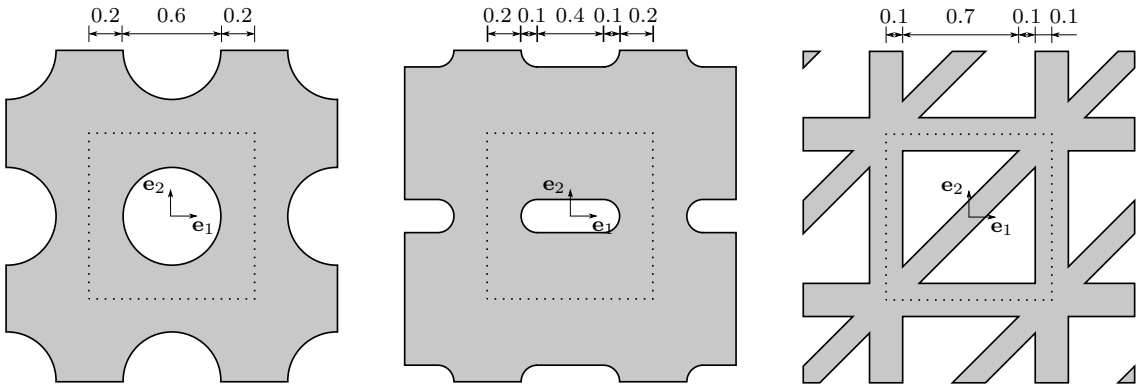

(a) circular (b) groove-shaped (c) diagonal

Figure 2.2: Sketch of different two-dimensional microstructures analysed with the electro-mechanically coupled multiscale finite element formulation. Reproduced from [42] under the terms of the Creative Commons Attribution 4.0 International License (CC BY 4.0).

caused by the evolution of microscale cracks. The contribution $\frac{\mathrm{d}\boldsymbol{j}_\mathrm{M}}{\mathrm{d}\boldsymbol{e}_\mathrm{M}}$, relating changes in the electric field vector to changes in the electric current density vector, can be identified with the macroscale conductivity tensor $\boldsymbol{\mathcal{S}}_\mathrm{M}$ and interpreted as a fingerprint of the microstructure.

As an example consider the microstructures depicted in Figure 2.2 and assume the linear constitutive relation

$$\boldsymbol{j} = \boldsymbol{\mathcal{S}} \cdot \boldsymbol{e} \tag{2.4}$$

for each microscale material point, with the isotropic conductivity tensor $\boldsymbol{\mathcal{S}} = \kappa\, \boldsymbol{I}$ being defined in terms of the scalar-valued conductivity κ. The application of the homogenisation scheme with periodic boundary conditions yields the macroscopic conductivity tensors

$$[\boldsymbol{\mathcal{S}}_\mathrm{M}]_{ij}^{\mathrm{cir}} = \begin{bmatrix} 0.56 & 0.00 \\ 0.00 & 0.56 \end{bmatrix} \kappa \quad , \quad [\boldsymbol{\mathcal{S}}_\mathrm{M}]_{ij}^{\mathrm{gro}} = \begin{bmatrix} 0.86 & 0.00 \\ 0.00 & 0.64 \end{bmatrix} \kappa \quad , \quad [\boldsymbol{\mathcal{S}}_\mathrm{M}]_{ij}^{\mathrm{dia}} = \begin{bmatrix} 0.31 & 0.07 \\ 0.07 & 0.31 \end{bmatrix} \kappa \tag{2.5}$$

with superscripts referring to the respective microstructure. Comparing the effective macroscopic conductivity tensor of a material with circular voids with the conductivity tensor of an idealised material, it is observed that the effective macroscopic constitutive response remains isotropic, whereas a reduction in the conductivity of approximately 44% is observed. In contrast, the effective macroscopic conductivity tensor that results from a microstructure with a groove-shaped void as depicted in Figure 2.2(b) is significantly anisotropic. However, the principal material axes are aligned with the $\mathbf{e}_1$- and $\mathbf{e}_2$-coordinate axes such that the conductivity tensor is in diagonal form. In the case of

the microstructure of diagonal type depicted in Figure 2.2(c), the $\mathbf{e}_1$- and $\mathbf{e}_2$-coordinate axes are not aligned with the principal material axes. Thus, the effective macroscopic conductivity tensor is not in diagonal form but features off-diagonal components.

The previous examples demonstrate the applicability of the electro-mechanical multiscale formulation to extract effective macroscopic conductivity tensors for given microstructures. Further examples focusing, amongst others, on the simulation of macroscale boundary value problems with spatially varying microstructures and on deformation-induced changes in the effective conductivity, e.g. caused by the evolution of microscale damage, are provided in **Paper 1**. In a finite deformation setting, severe changes in the microscale morphology, for instance associated with the shape of microscale pores, result in an additional coupling of the electrical and mechanical field equations. These effects are in the focus of the finite deformation multiscale approach developed in **Paper 2** and are discussed in Section 2.1.2.

2.1.2 Finite deformation setting

In analogy with the developments in an infinitesimal deformation setting, the governing set of field equations under the assumptions of quasi-statics and quasi-stationarity consists of the balance equation of linear momentum and the continuity equation for the electric charge. With respect to the referential configuration they take the form

$$\nabla_{\boldsymbol{X}} \cdot \boldsymbol{P} = \boldsymbol{0} \quad , \qquad (2.6a) \qquad \nabla_{\boldsymbol{X}} \cdot \boldsymbol{J} = 0 \quad , \qquad (2.6b)$$

where $\boldsymbol{P}$ denotes the first Piola-Kirchhoff stress tensor and $\boldsymbol{J}$ the referential electric current density vector. These tensors require constitutive specification and are, in general, functions of the deformation gradient $\boldsymbol{F}$, the referential electric field vector $\boldsymbol{E}$ and internal variables. Similar to mechanical problems, the electrical sub-problem can be formulated with respect to referential or spatial quantities which are related via push- and pull operations according to

$$\boldsymbol{J} = \det(\boldsymbol{F})\ \boldsymbol{F}^{-1} \cdot \boldsymbol{j} \ , \qquad (2.7a) \qquad \boldsymbol{E} = \boldsymbol{F}^{\mathrm{t}} \cdot \boldsymbol{e} \ . \qquad (2.7b)$$

Moreover, it is noted that the referential and spatial electric field vectors are derivable from the electric potential field as

$$\boldsymbol{E} = -\nabla_{\boldsymbol{X}} \phi \ , \qquad (2.8a) \qquad \boldsymbol{e} = -\nabla_{\boldsymbol{x}} \phi \ , \qquad (2.8b)$$

hold, with subscripts indicating derivatives with respect to referential and spatial coordinates.

In paper **Paper 2**, a computational multiscale formulation for electrical conductors in a finite deformation setting is proposed where the phenomenological constitutive re-

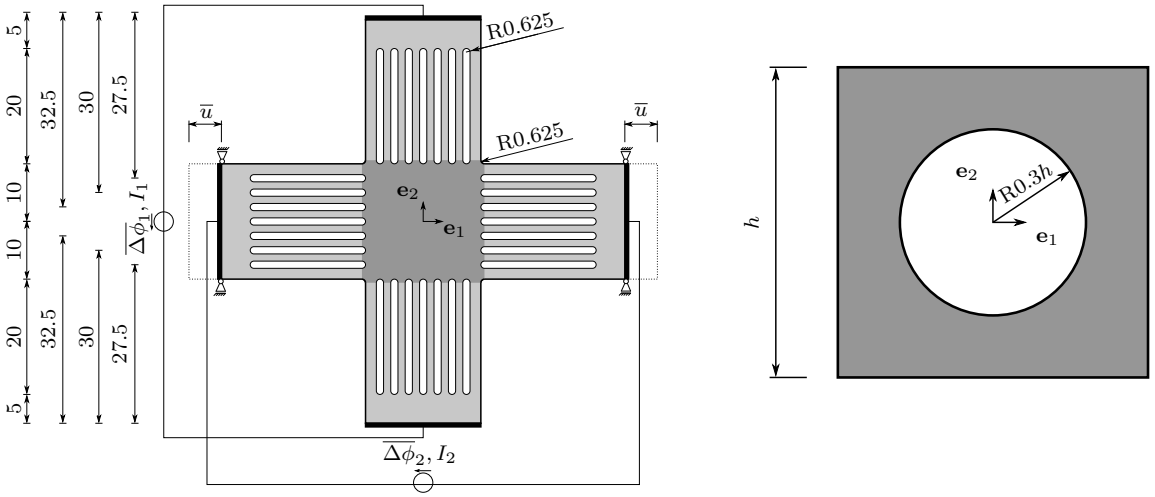

(a) macroscale (b) microscale

Figure 2.3: Biaxial tensile test specimen used in the electro-mechanically coupled multiscale simulations. Microstructural imperfections according to b) are assumed in the dark grey coloured region and resolved by using the proposed multiscale approach. In the light grey coloured region, a classic phenomenological material model is used. Dimensions are given in mm. Reproduced from [43] under the terms of the Creative Commons Attribution 4.0 International License (CC BY 4.0).

lations at the macroscale, relating stresses to strains and electric current densities to the electric field, are substituted by the solution of a microscale boundary value problem. To this end, the respective scale-bridging relations are established, a finite element-based implementation is developed and representative boundary value problems are analysed so as to reveal principal model properties of the proposed formulation.

For demonstration purposes a Neo-Hookean-type energy potential and a linear relation between the (spatial) electric current density vector and the (spatial) electric field vector, namely,

$$\boldsymbol{j} = \boldsymbol{\mathcal{S}}_t \cdot \boldsymbol{e} \quad , \tag{2.9}$$

are adopted at the microscale. In (2.9), $\boldsymbol{\mathcal{S}}_t$ denotes the positive (semi-)definite spatial conductivity tensor that is chosen to be constant, isotropic, and to depend on the scalar-valued conductivity parameter κ_t, i.e. $\boldsymbol{\mathcal{S}}_t = \kappa_t \boldsymbol{I}$. By additionally invoking (2.7), the referential representation of (2.9) follows as

$$\boldsymbol{J} = \left[J_{\boldsymbol{F}} \boldsymbol{F}^{-1} \cdot \boldsymbol{\mathcal{S}}_t \cdot \boldsymbol{F}^{-\mathrm{t}} \right] \cdot \boldsymbol{E} \quad . \tag{2.10}$$

Assuming κ_t to be constant allows us to study the influence of finite geometry changes at the microscale (e.g. of voids) on the effective electrical conductivity tensor at the macroscale. To this end, focus is on the biaxial tensile test specimen depicted in Figure 2.3(a). The specimen consists of two different materials as indicated in light and dark grey. In the dark grey coloured region, a material microstructure with a circular void

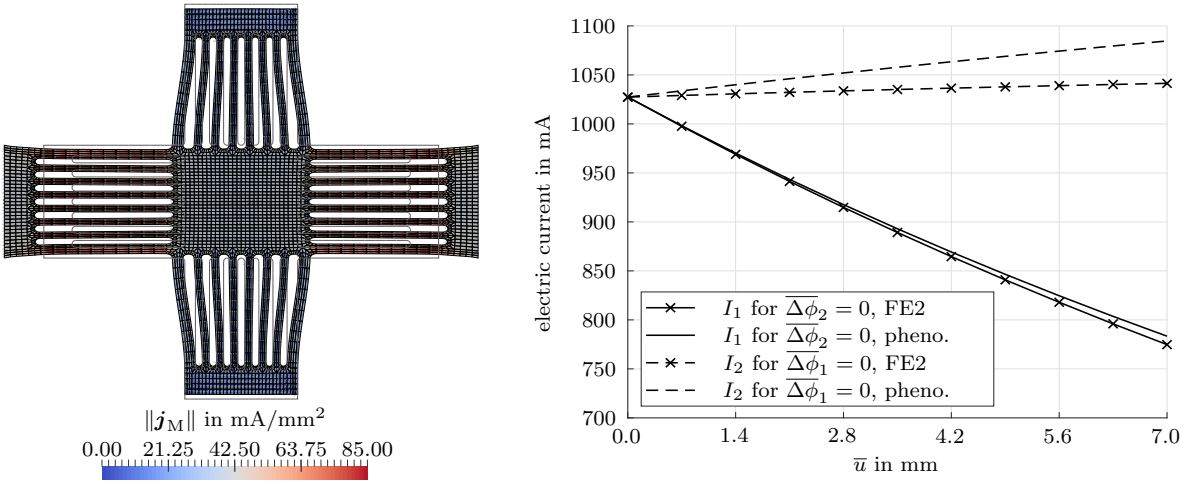

(a) macroscale simulation results

(b) electric current as a function of deformation

Figure 2.4: a) Deformation and electric current density for the biaxial tensile test specimen according to Figure 2.3 with $\overline{u} = 7.0\,\mathrm{mm}$, $\overline{\Delta\phi}_1 = 0.1\,\mathrm{mV}$ and $\overline{\Delta\phi}_2 = 0.0\,\mathrm{mV}$. The outline of the reference configuration is depicted in light grey colour and grey coloured arrows indicate the direction of the electric current. b) Electric current $I_\bullet$ as a function of deformation for a prescribed electric potential difference $\overline{\Delta\phi}_\bullet = 0.1\,\mathrm{mV}$. Curves labelled with "FE2" indicate fully coupled electro-mechanical multiscale simulations. Curves labelled with "pheno." indicate reference solutions with a multiscale approach used for the mechanical problem and a classic phenomenological material model with a constant spatial conductivity tensor used for the electrical problem. Reproduced from [43] under the terms of the Creative Commons Attribution 4.0 International License (CC BY 4.0).

according to Figure 2.3(b) is assumed, and the effective macroscopic material behaviour is calculated by using the proposed multifield multiscale formulation. In the light grey coloured region, an idealised material behaviour representing a microstructure without voids is assumed. The specimen is loaded in $\mathbf{e}_1$-direction, with the prescribed horizontal displacement $\overline{u}$ being linearly increased and the vertical displacement enforced to be zero at both ends. The remaining boundaries are assumed to be traction-free. Regarding the electrical subproblem either a potential difference $\overline{\Delta\phi}_1$ or a potential difference $\overline{\Delta\phi}_2$ is prescribed. The remaining boundaries are assumed to be electrically insulated.

A reference model is introduced in order to evaluate the influence of the microscale deformation on the effective macroscopic quantities that may be measured in experiments. This model does not take changes in the effective conductivity tensor due to deformation processes at the microscale into account. However, the mechanical behaviour is still assumed to be governed by the microscale so that the macroscopic deformation is the same as in the fully-coupled FE^2-model. To this end, the FE^2-based calculation of the electrical subproblem in the dark grey coloured region is replaced by a classic single-scale material model with the effective spatial conductivity tensor $\widetilde{\boldsymbol{\mathcal{S}}}_{\mathrm{M}t} = \widetilde{\kappa}_t\, \boldsymbol{I}$ that resembles the properties of the microstructure in the undeformed state. The respective elongation-electric current curves are provided in Figure 2.4: 1) By comparing the $\overline{\Delta\phi}_1 = 0.1\,\mathrm{mV}$

and $\overline{\Delta\phi}_2 = 0.1\,\mathrm{mV}$ curves, a significant difference in the electric current is observed that can primarily be attributed to the macroscopic deformation process. In particular, the effective electrical resistance in $\mathbf{e}_1$-direction increases because the length of the specimen increases while the effective cross section is reduced. Likewise, the effective electrical resistance in $\mathbf{e}_2$-direction decreases. 2) Regarding the difference between FE^2-based simulations (that account for the influence of the inhomogeneous microscale deformation on the effective macroscopic conductivity tensor) and the reference model as defined above (that does not account for deformation-induced changes in the conductivity tensor), one observes a significant decrease in the electric current with increasing deformation for the complete FE^2 model.

The simulation results demonstrate the capability of the proposed multiscale formulation to account for mechanically-induced changes in the effective electrical conductivity and to predict the response of a macroscale specimen with a spatially varying, evolving microstructure. With the electro-mechanically coupled multiscale formulations at hand, focus is laid on the application to and the comparison with experiments in Section 2.2.

2.2 Application to and comparison with experiments

The applicability of the computational multiscale scheme proposed in **Paper 1** is studied in this section by taking experimental data into account. To this end, the influence of artificially generated, geometrically well-defined microscale pores (**Paper 3**) and of deformation-induced microscale cracks (**Paper 4**) on the effective electrical conductivity is exemplarily analysed in Section 2.2.1 and Section 2.2.2, respectively.

2.2.1 Probing porosity in metals by electrical conductivity

Paper 3 deals with a detailed study of conductivity changes caused by the presence of sub-microscale pores. Reducing the complexity of the material system, geometrically well-defined pore arrays are created by focused ion beam (FIB) milling in Cu thin films and characterised by 4-point probe electrical measurements. Specifically speaking, four needles approach the surface of the sample as shown in Figure 2.5. The outer needles supply the electric current and are in a fixed position during the experiment. The inner needles are used to measure the voltage drop along the measurement line.

The experiment is designed such that an overall (quasi-)unidirectional electric current is observed that is, however, strongly inhomogeneous in the region where the microstructural imperfections are induced. Motivated by Saint-Venant's principle of mechanical problems, it is thus proposed to measure the electric potential difference at a distance from the imperfections and to evaluate their influence on the overall electrical material properties by using the equivalent model sketched in Figure 2.6.

More specifically speaking, the electric potential difference $\Delta\phi$ between the points B and C that are a distance $l_\phi < l_I$ apart is in a first step measured for a prescribed

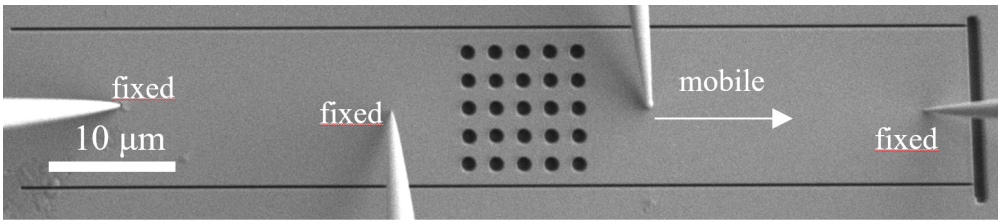

(a) experimental setup

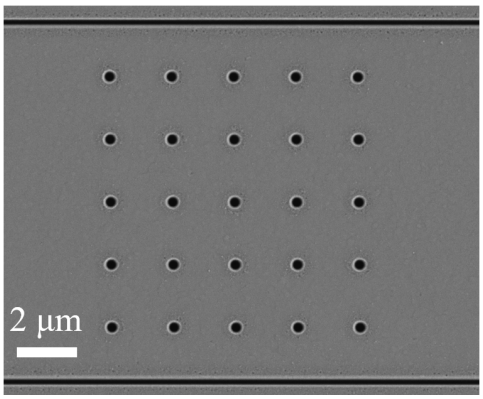

(b) $d_\square = 420\,\mathrm{nm}$

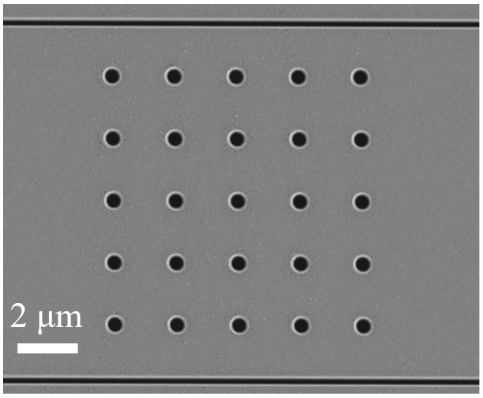

(c) $d_\square = 515\,\mathrm{nm}$

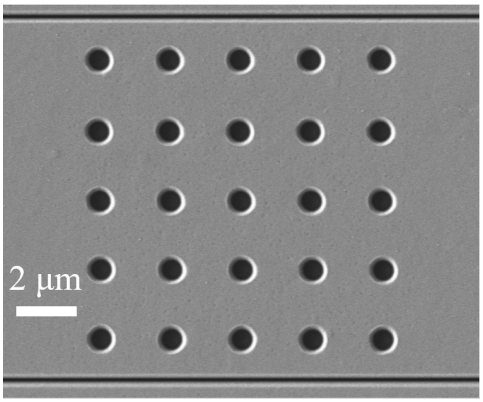

(d) $d_\square = 660\,\mathrm{nm}$

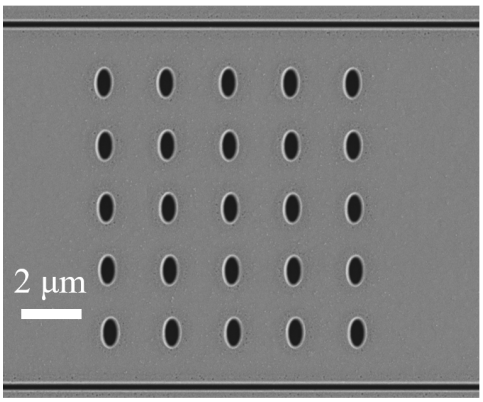

(e) $a_\square = 950\,\mathrm{nm}$, $b_\square = 510\,\mathrm{nm}$

Figure 2.5: Experimental setup and artificially created microstructures featuring circular pores of diameter $d_\square$ and elliptical pores with principal axes $\{a_\square, b_\square\}$, respectively. Reproduced from [46] under the terms of the Creative Commons Attribution 4.0 International License (CC BY 4.0).

electric current I. In a second step, the experimental data is compared with simulation results that are based on series and parallel connections of resistors as sketched out in Figure 2.6(b). In addition to the effective resistance $R_\square$ associated with the $n_\square \times n_\square$ array of unit cells, the resistance caused by the material region of length l_-, i.e. R_-, and the resistance associated with the material region of height $h_|$, i.e. $R_|$, are accounted for. In this regard, it is noted that the geometric dimensions are directly extracted from

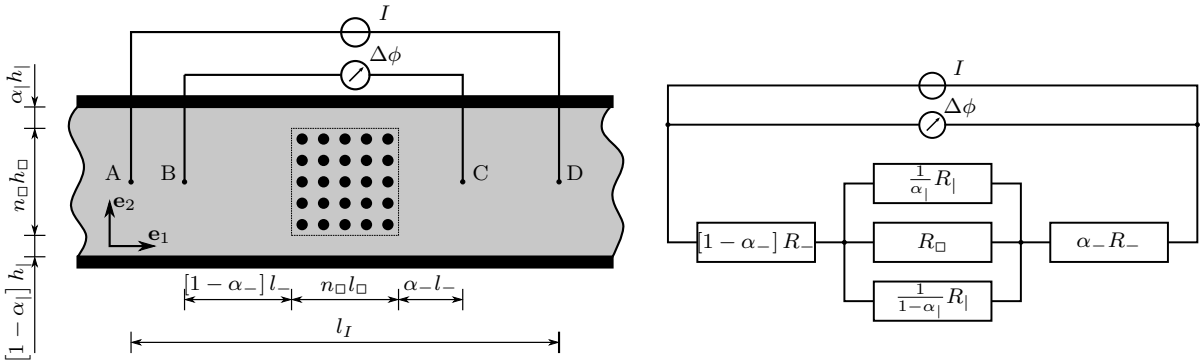

(a) experimental setup (b) equivalent model

Figure 2.6: Experimental setup and modelling approach with $0 \leq \alpha_- \leq 1$, $0 \leq \alpha_| \leq 1$ and $l_\phi = n_\square l_\square + l_-$. The material and structural properties do not significantly vary over the thickness t, such that a two-dimensional modelling approach is taken. Reproduced from [46] under the terms of the Creative Commons Attribution 4.0 International License (CC BY 4.0).

the experimental images. The remaining unknowns that occur in the calculation of the potential difference

$$\begin{aligned}\Delta\phi\left(l_\phi\right) &\approx \left[R_- + \left[\frac{1}{R_\square} + \frac{1}{R_|}\right]^{-1}\right] I \\ &= \left[\frac{1}{\kappa}\frac{l_\phi - n_\square l_\square}{\left[h_| + n_\square h_\square\right] t} + \left[\kappa_\square \frac{h_\square t}{l_\square} + \kappa \frac{h_| t}{n_\square l_\square}\right]^{-1}\right] I\end{aligned} \tag{2.11}$$

are the scalar-valued conductivity κ of the base material, and the effective conductivity (in $\mathbf{e}_1$-direction) of the material region that features pores, $\kappa_\square$. Conductivity coefficient $\kappa_\square$ is, however, not independent but can be related to the conductivity of the base material by making use of the computational homogenisation scheme proposed in **Paper 1** and by projecting the homogenised conductivity tensor $\boldsymbol{\mathcal{S}}_\mathrm{M}$ into the $\mathbf{e}_1$-direction,

$$\kappa_\square = \mathbf{e}_1 \cdot \boldsymbol{\mathcal{S}}_\mathrm{M} \cdot \mathbf{e}_1 \quad . \tag{2.12}$$

Accordingly, by making use of the computational homogenisation scheme and by introducing the conductivity ratio

$$\beta_\square = \kappa_\square / \kappa \tag{2.13}$$

that measures the influence of the pore-type inclusions on the effective resistivity, relation (2.11) can be recast in the form

$$\Delta\phi\left(l_\phi\right) \approx \left[\frac{l_\phi - n_\square l_\square}{\left[h_| + n_\square h_\square\right] t} + \left[\beta_\square \frac{h_\square t}{l_\square} + \frac{h_| t}{n_\square l_\square}\right]^{-1}\right] \frac{I}{\kappa} \quad . \tag{2.14}$$

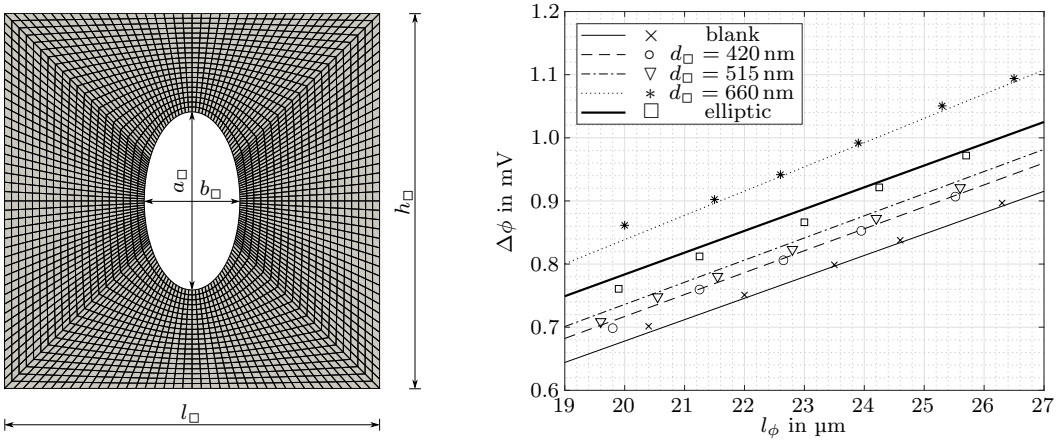

(a) unit cell with elliptic inclusion (b) experiments and simulation results

Figure 2.7: Comparison of experiment and simulation: a) Finite element discretised unit cell with elliptic inclusion ($l_\square = h_\square = 2000\,\mathrm{nm}$, $a_\square = 950\,\mathrm{nm}$, $b_\square = 510\,\mathrm{nm}$) b) Experimentally determined ($\times, \circ, \triangledown, *, \square$) and simulated ($-, --, -\cdot, \cdot\cdot, -$) potential difference as a function of contact distance. Simulation results for $I = 10\,\mathrm{mA}$ and $\kappa = 51.3\,\mathrm{mA/mV\mu m}$ are shown. Reproduced from [46] under the terms of the Creative Commons Attribution 4.0 International License (CC BY 4.0).

To study the applicability of the computational homogenisation scheme for electrical conductors, finite element discretised unit cells as exemplarily shown in Figure 2.7(a) are, in a first step, prepared from the experimental images shown in Figure 2.5. Based on these, effective conductivity tensors and conductivity ratios are calculated in a second step by application of the computational homogenisation scheme.

In addition to the microstructures with pores shown in Figure 2.5, an ideal Cu thin film is taken into account as a reference. For all samples, a spatially uniform thickness is assumed and the geometric dimensions are extracted from the experimental images. With these data at hand and for the particular choice $\kappa = 51.3\,\mathrm{mA/mV\mu m}$ that is based on the direct measurement of the pristine thin-film, the evaluation of (2.14) yields the $\Delta\phi$-l_ϕ-curves depicted in Figure 2.7(b).

In addition, the experimentally obtained data points are provided in Figure 2.7(b). As expected, it is observed that the measured voltage-drop between the inner needles increases with the distance between the contacts and that the measured voltage-drop scales with the dimensions of the pores. Overall, experiment and simulation agree well, both quantitatively and qualitatively, which shows both: the accuracy of the electrical measurements and the applicability of the proposed modelling approach.

2.2.2 Predicting effective properties of metal thin films

Paper 3 dealt with a multiscale study of artificially generated microstructures to gain a detailed understanding of the proposed multiscale approach when applied to ex-

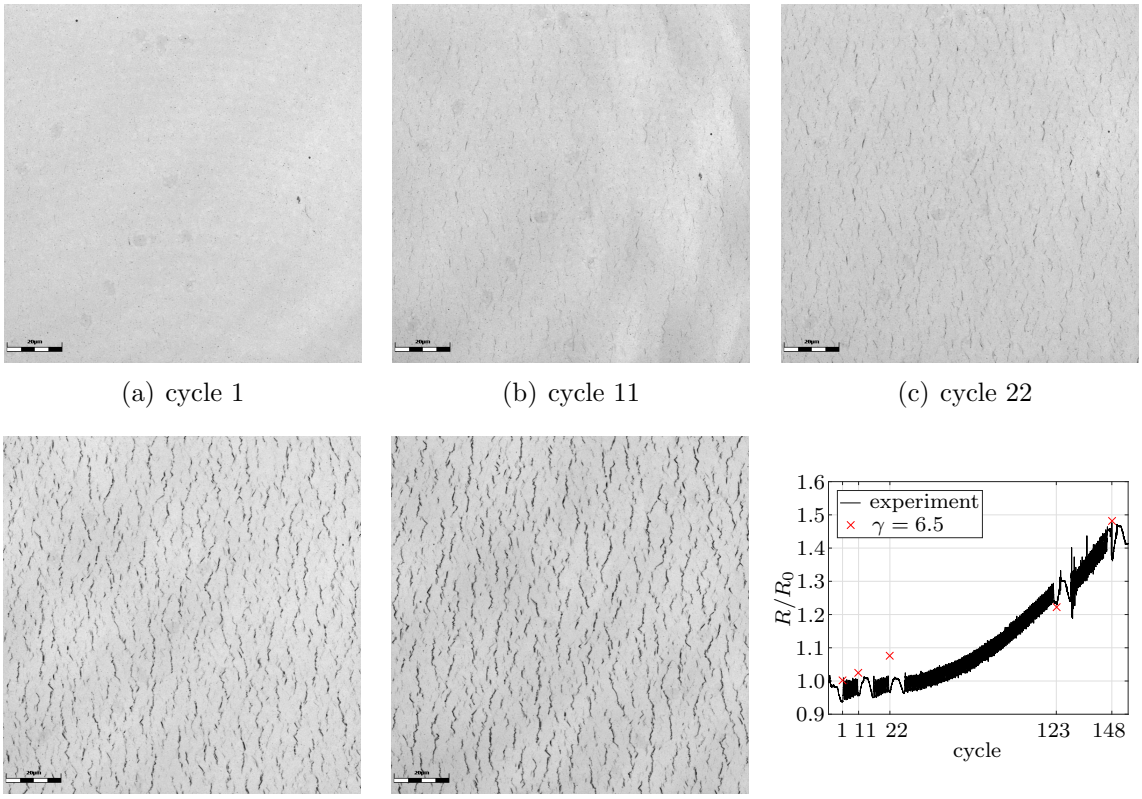

(a) cycle 1 (b) cycle 11 (c) cycle 22

(d) cycle 123 (e) cycle 148 (f) relative resistance ratio

Figure 2.8: a-e) Laser intensity images for different deformation states of a 200 nm Cu film with a 10 nm Cr adhesion layer on a 50 µm thick Upilex Polyimide substrate (130 µm × 130 µm micrographs). The tensile straining was parallel to the horizontal direction and all scale bars are 20 µm. f) Experimentally recorded relative resistance ratio as a function of load cycles and multiscale simulation results for $\gamma = 6.5$. Reproduced from [41] under the terms of the Creative Commons Attribution 4.0 International License (CC BY 4.0).

periments. These developments are extended in **Paper 4** where the focus is laid on deformation-induced microscale cracks in metallic thin films.

To this end a bilayer made of a 200 nm Cu film with a 10 nm Cr adhesion layer on a 50 µm Upilex Polyimide substrate is cyclically strained and analysed by using four point probe resistance measurements and confocal laser scanning microscopy (CLSM) imaging. For the in-situ electrical measurements, the relative resistance ratio, R/R_0, is used where R_0 is the initial resistance before straining (without mechanical damage or cracks) and where R is the instantaneous measured resistance. The relative resistance ratio as a function of the load cycle number is depicted in Figure 2.8(f) and exemplary laser intensity images that are the basis for the subsequent developments are shown in Figure 2.8 (a-e).

The geometric data from the CLSM laser intensity images is converted into finite element meshes, which serve as the basis for the computational homogenisation scheme.

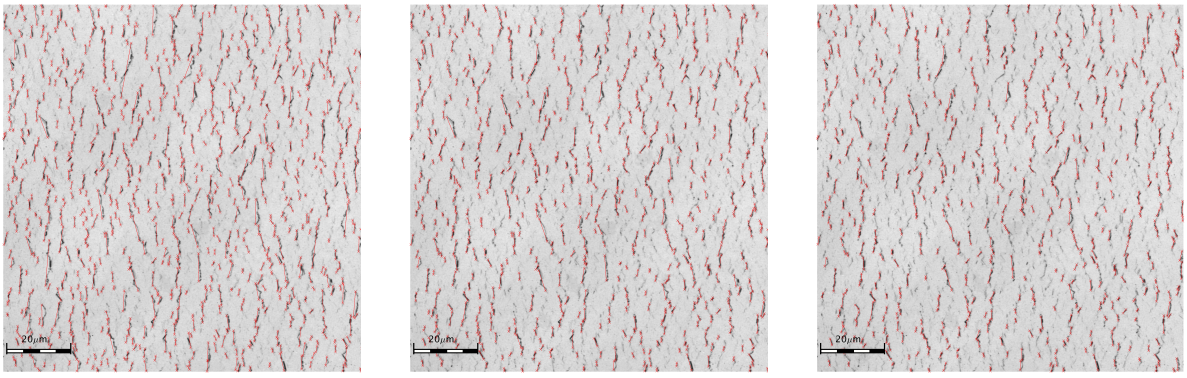

(a) cycle 123, $\gamma = 4.0$ (b) cycle 123, $\gamma = 6.5$ (c) cycle 123, $\gamma = 8.0$

Figure 2.9: Comparison of identified cracks using three different filter options. Depicted are 114 µm × 114 µm micrographs for $\gamma \in \{4.0, 6.5, 8.0\}$ with red lines indicating the cracks that have been identified. Reproduced from [41] under the terms of the Creative Commons Attribution 4.0 International License (CC BY 4.0).

Being more specific, greyscale gradients in loading direction ($\mathbf{e}_1$) of the micrographs depicted in Figure 2.8 are calculated in a first step, since the cracks preferably form in the transverse direction ($\mathbf{e}_2$). In a second step, only pixels with negative greyscale gradient values that are higher than a factor γ times the mean value of the negative greyscale gradients in loading direction are considered to represent cracks. This condition can be stated as

$$-\nabla \mathcal{G}_i \cdot \mathbf{e}_1 > \gamma \frac{1}{\mathrm{n_{pix}}} \sum_{j=1}^{\mathrm{n_{pix}}} \max\left\{0, -\nabla \mathcal{G}_j \cdot \mathbf{e}_1\right\} \quad , \tag{2.15}$$

with $\mathcal{G}_\bullet$ denoting the greyscale value of pixel $\bullet$ and with $\mathrm{n_{pix}}$ denoting the number of pixels in the image. By additionally applying morphological operations, representative volume elements with geometrically resolved cracks as exemplarily shown in Figure 2.9 are prepared from the experimental images, and effective conductivity tensors $\boldsymbol{\mathcal{S}}_{\mathrm{M}}^{\bullet}$ are extracted for each load step $\bullet$. In accordance with the (quasi-one-dimensional) model problem depicted in Figure 1.3, in view of the experimental results presented in Figure 2.8(f), and by taking into account that

$$\frac{R}{R_0} = \frac{\kappa_0}{\kappa} \frac{L}{L_0} \frac{A_0}{A} \approx \frac{\mathbf{e}_1 \cdot \boldsymbol{\mathcal{S}}_{\mathrm{M}}^{0} \cdot \mathbf{e}_1}{\mathbf{e}_1 \cdot \boldsymbol{\mathcal{S}}_{\mathrm{M}}^{\bullet} \cdot \mathbf{e}_1} \frac{L}{L_0} \frac{A_0}{A} \tag{2.16}$$

holds for a quasi one-dimensional setting, the simulation results are normalised with respect to an idealised material which does not contain cracks at the microscale.

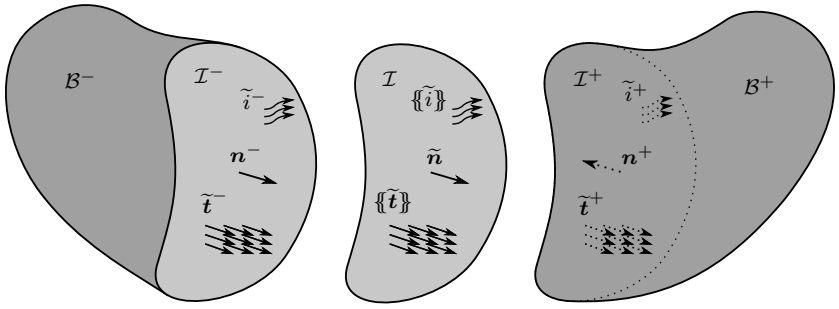

Figure 2.10: Specification of quantities in the continuum $\mathcal{B}$ and at the interface $\mathcal{I}$. Reproduced from [40] under the terms of the Creative Commons Attribution 4.0 International License (CC BY 4.0).

The experimental data and the relative resistance ratios that were calculated by means of multiscale finite element simulations are provided in Figure 2.8(f). In general, and especially for high cycle numbers, experiment and simulation are in good agreement. However, there is an interesting difference at cycle 22 which suggests that for small cycle numbers too many regions have been associated with through-thickness cracks which leads to an increase in the predicted relative resistance ratio. Comparing the corresponding micrograph of cycle 22 shown in Figure 2.8(c) with the images corresponding to higher cycle numbers, e.g. Figure 2.8(d) or Figure 2.8(e), it is observed that the greyscale gradients are much less pronounced. Accordingly, this observation underlines the need for further experimental and simulation based analyses in future works, in order to reliably distinguish between through-thickness cracks and plastic localisation zones. Nevertheless, the comparison of simulation results and experimental findings clearly demonstrates the usefulness of the proposed multiscale formulation in relating deformation-induced microscale cracks to macroscopic electrical properties of metal thin films.

2.3 Modelling of material interfaces

In Sections 2.1 and 2.2, and in the corresponding publications **Paper 1**–**Paper 4** focus was laid on the prediction of effective electrical properties of, possibly evolving, microstructures by making use of computational multiscale approaches. The quality of the predictions in these approaches intrinsically relies on accurate material models that have been developed at the level of individual phases. In this regard, it was observed in the experimental studies summarised in Figure 1.4 that material interfaces at the microscale and related mechanically-induced failure processes such as decohesion and crack propagation may have a significant influence on the overall material response. These effects are in the focus of **Paper 5** that deals with the fundamentals of electro-mechanically coupled cohesive zone formulations for electrical conductors.

At the outset of the developments, the governing set of partial differential equations and jump conditions that characterises (thermo-)electro-mechanical processes in a continuum with material interfaces is derived. The continuum is sketched out in Figure 2.10 with superscript $\bullet^+$ and $\bullet^-$ referring to quantities at opposing sides of the interface $\mathcal{I}$. The interface itself is characterised by its unit surface normal vector $\widetilde{\boldsymbol{n}}$, the jump of a quantity across the interface is defined as $[\![\bullet]\!] = \bullet^+ - \bullet^-$ and the interfacial mean value reads $\{\!\{\bullet\}\!\} = \frac{1}{2}\left[\bullet^+ + \bullet^-\right]$. With these definitions at hand and by introducing the traction vector $\widetilde{\boldsymbol{t}} = \boldsymbol{\sigma} \cdot \widetilde{\boldsymbol{n}}$, the mechanical subproblem for a quasi-static quasi-stationary setting and negligible body forces takes the form

$$\nabla \cdot \boldsymbol{\sigma} = \boldsymbol{0} \quad \text{(in the bulk)} \quad , \tag{2.17a}$$

$$[\![\widetilde{\boldsymbol{t}}]\!] = \boldsymbol{0} \quad \text{(at the interface)} \quad . \tag{2.17b}$$

The electrical subproblem reduces to the continuity equation for the electric charge

$$\nabla \cdot \boldsymbol{j} = 0 \quad \text{(in the bulk)} \quad , \tag{2.18a}$$

$$[\![\widetilde{i}]\!] = 0 \quad \text{(at the interface)} \quad , \tag{2.18b}$$

with $\widetilde{i} = \boldsymbol{j} \cdot \widetilde{\boldsymbol{n}}$ denoting the projected current density vector, and to Faraday's law of induction which can naturally be fulfilled by the introduction of an electric potential field ϕ such that $\boldsymbol{e} = -\nabla\phi$. The balance equation of energy takes the form

$$\rho\,\dot{e} = \boldsymbol{\sigma} : \dot{\boldsymbol{\varepsilon}} \qquad + \boldsymbol{j} \cdot \boldsymbol{e} \qquad - \nabla \cdot \boldsymbol{q} \qquad \text{(in the bulk)}, \tag{2.19a}$$

$$\widetilde{\rho}\,\dot{\widetilde{e}} = [\![\dot{\boldsymbol{u}}]\!] \cdot \{\!\{\widetilde{\boldsymbol{t}}\}\!\} - \{\!\{\widetilde{i}\}\!\}\,[\![\phi]\!] - [\![\boldsymbol{q} \cdot \widetilde{\boldsymbol{n}}]\!] \qquad \text{(at the interface)} \ , \tag{2.19b}$$

where e and $\widetilde{e}$ denote (mass-specific) internal energy densities, ρ and $\widetilde{\rho}$ mass densities, $\boldsymbol{\varepsilon}$ the small strain deformation tensor, $\boldsymbol{q}$ the heat flux vector and $\boldsymbol{u}$ the displacement vector. By additionally introducing (mass-specific) free energy density functions ψ and $\widetilde{\psi}$, entropy densities s and $\widetilde{s}$, and absolute temperatures θ and $\widetilde{\theta}$, the dissipation inequality takes the form

$$\boldsymbol{\sigma} : \dot{\boldsymbol{\varepsilon}} \qquad - \rho\left[\dot{\psi} + s\,\dot{\theta}\right] + \boldsymbol{j} \cdot \boldsymbol{e} \qquad - \frac{1}{\theta}\,\boldsymbol{q} \cdot \nabla\theta \geq 0 \qquad \text{(in the bulk)} \tag{2.20a}$$

$$[\![\dot{\boldsymbol{u}}]\!] \cdot \{\!\{\widetilde{\boldsymbol{t}}\}\!\} - \widetilde{\rho}\left[\dot{\widetilde{\psi}} + \widetilde{s}\,\dot{\widetilde{\theta}}\right] - \{\!\{\widetilde{i}\}\!\}\,[\![\phi]\!] + \widetilde{\theta}\left[\{\!\{\boldsymbol{q} \cdot \widetilde{\boldsymbol{n}}\}\!\}\,[\![\theta^{-1}]\!] + \left[\{\!\{\theta^{-1}\}\!\} - \widetilde{\theta}^{-1}\right][\![\boldsymbol{q} \cdot \widetilde{\boldsymbol{n}}]\!]\right] \geq 0$$
$$\text{(at the interface)} \ . \tag{2.20b}$$

With the governing set of balance relations (2.17)-(2.20) at hand, a thermodynamically consistent cohesive zone formulation that accounts for the influence of interfacial damage processes on the electrical conductivity is developed in **Paper 5**. As to reveal principal properties of the proposed formulation, an isotropic linear elastic response and a constant isotropic conductivity tensor are assumed in the bulk. At the interface, a linear elastic relation combined with a classic energy-driven $1-\widetilde{d}$ damage formulation is adopted under tension, whereas the interface is assumed to regain its initial stiffness un-

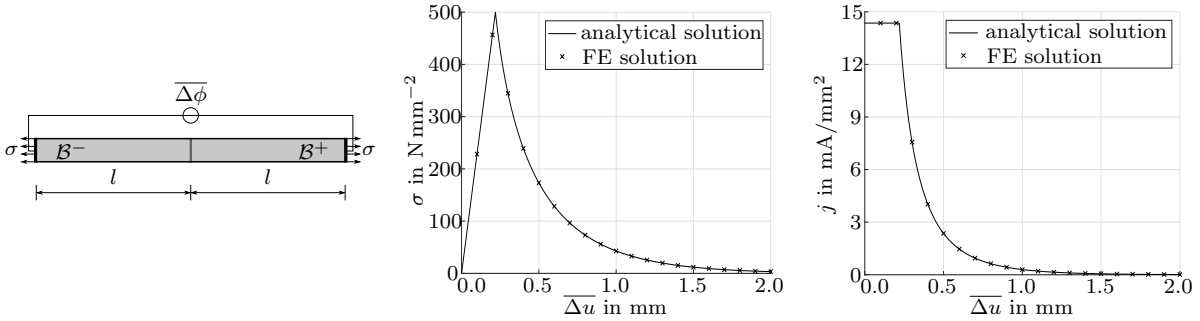

(a) boundary value problem (b) axial stress (c) axial electric current density

Figure 2.11: Bar of length $2\,l$ and cross-sectional area A, subjected to mechanical and electrical loadings. A material interface is positioned in the middle of the bar as indicated by dark grey colour. Analytical solutions and two-dimensional finite element simulation results for the axial stress σ and axial electric current density j as functions of deformation are provided. Reproduced from [40] under the terms of the Creative Commons Attribution 4.0 International License (CC BY 4.0).

der compression. Moreover, the deformation-induced damage processes at the interface are assumed to influence the electrical conductivity. The specific form of the constitutive equation for the electric current density

$$\{\!\{\widetilde{i}\}\!\} = \begin{cases} -\left[1-\widetilde{d}\right]\widetilde{\kappa}\,[\![\phi]\!] & \text{if } [\![\boldsymbol{u}]\!]\cdot\widetilde{\boldsymbol{n}} > 0 \quad \text{(tension)} \\ -\widetilde{\kappa}\,[\![\phi]\!] & \text{if } [\![\boldsymbol{u}]\!]\cdot\widetilde{\boldsymbol{n}} \leq 0 \quad \text{(compression)} \end{cases} , \tag{2.21}$$

with $\widetilde{\kappa}$ denoting the idealised conductivity of the interface, thus establishes a coupling between the electrical and mechanical field equations.

As a first example, consider the bar depicted in Figure 2.11(a) that is subjected to a prescribed elongation $\overline{\Delta u}$ and potential difference $\overline{\Delta\phi}$. For monotonic tensile loadings, the quasi-one-dimensional boundary value problem is amendable to analytical techniques. The respective load-displacement- and electric current density-displacement curves predicted by a finite element-based simulation are shown together with their analytical counterparts in Figures 2.11(b) and 2.11(c). After the onset of damage evolution, significant decreases in stiffness and conductivity with increasing deformation are observable which demonstrates: a) the influence of the material interface on the overall properties of the sample and b) the coupling between the electrical and mechanical field equations via the damage variable $\widetilde{d}$.

As a second example, focus is laid on the polycrystalline specimen depicted in Figure 2.12, where the grain boundaries are resolved by making use of the proposed cohesive zone formulation. In a first load step, the sample is subjected to tensile loading which causes the evolution of interface damage. In a second load step the loading is reversed, leading to a compressive load state. The different configurations and the electric potential field distributions depicted in Figure 2.12 exemplify: a) the predicted intergranular

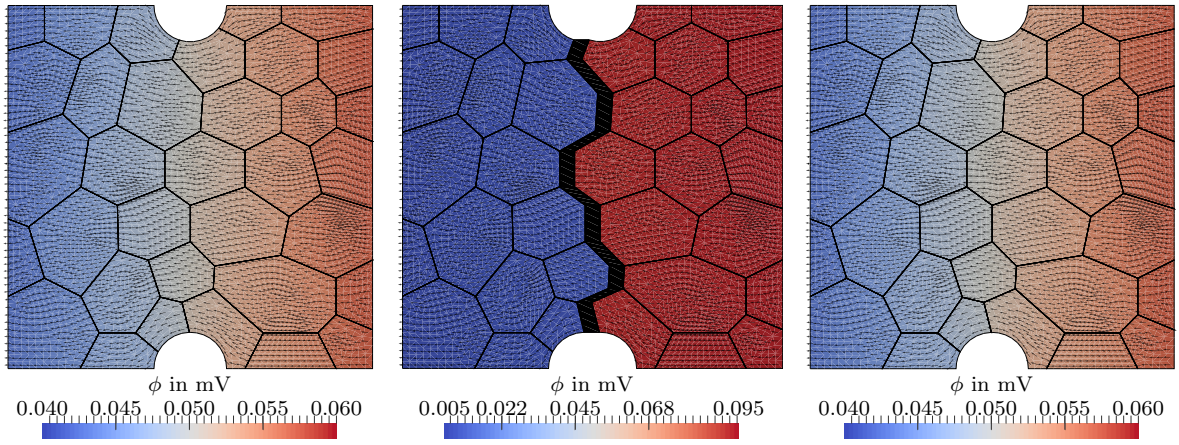

(a) reference state (b) tensile state (c) compressive state

Figure 2.12: Electric potential field ϕ for a polycrystalline specimen under various loading conditions. It is noted that the material interface in c) is damaged due to the deformation history. Normalised electric current density vectors are indicated by black arrows. Reproduced from [40] under the terms of the Creative Commons Attribution 4.0 International License (CC BY 4.0).

crack propagation, b) the reduction in conductivity caused by the evolution of interface damage and c) the recovery of the initial conductivity under compressive load states.

2.4 Wavelet approaches to the solution of microscale boundary value problems

The detailed resolution of the material microstructure in computational multiscale methods is associated with a severe computational effort in terms of CPU time and memory requirements. This particularly holds true for the coupled problems considered in **Paper 1**–**Paper 4** and when sophisticated material models, such as the cohesive zone formulation developed in **Paper 5**, are used at the microscale. Against this background, tailored solution approaches to microscale boundary value problems are developed. Amongst those are FFT-based spectral solvers and wavelet-based approaches that are in the focus of **Paper 6** and **Paper 7**. Specifically speaking, **Paper 6** (Section 2.4.1) focuses on the fundamental properties of wavelet-based approaches when applied in the context of multiscale mechanics, and **Paper 7** (Section 2.4.2) discusses a hybrid wavelet-FFT approach for the efficient solution of microscale boundary value problems.

2.4.1 Adaptive wavelet-based collocation method

There are but a few works available in the literature that focus on the development and application of tailored wavelet-based approaches for continuum mechanics problems that

include non-linear history-dependent material behaviour. In particular, detailed studies of wavelet-based solution approaches in the context of multiscale mechanics are, to the author's best knowledge, not available despite the multiresolution property of wavelets which seems promising to properly resolve (possibly evolving) microscale features in representative volume elements. Against this background, the fundamental properties of a wavelet-based collocation approach in the context of computational homogenisation-based multiscale mechanics are studied in **Paper 6**. To this end, an in-depth analysis of elementary one-dimensional problems that occur in multiscale mechanics and for which analytical solutions can be furnished for validation purposes is carried out. Particular focus is laid on irreversible material behaviour and on microstructures that feature material interfaces and material interphases, respectively. The following key observations are made:

O1 (*Adaptivity*): It is shown that the chosen wavelet coefficient-based refinement algorithm is capable of dynamically adapting the numerical grid to the solution profile. In particular, the numerical grid is automatically refined close to material interfaces and interphases – i.e. in regions where significant changes in the solution profile are expected based on the phase-contrast – and close to deformation-induced elasto-plastic transition zones. Hence, the hierarchical character of wavelet-based approaches and the naturally occurring local refinement characteristics allow for an accurate representation of localised changes in the microscale fields.

O2 (*State variables*): It is shown that the proposed wavelet-based approach naturally gives rise to a mapping algorithm for state variables and does not require intricate patch-recovery techniques that are for instance used in FE-based schemes.

O3 (*Scale transition*): It is shown that the vanishing moment property of the lifted-interpolating wavelet family considered leads to an efficient integration of the domain and, hence, to an efficient computational homogenisation scheme. Moreover, a closed-form relation for the macroscale algorithmic consistent tangent stiffness tensor can be derived.

O4 (*Hill-Mandel condition*): It is shown that by accounting for the periodicity of microscale fields in wavelet synthesis and wavelet analysis operations the Hill-Mandel consistency condition can naturally be accounted for.

O5 (*Meshfree method*): The proposed wavelet-based approach is intrinsically mesh-free which allows experimental pixel-based data to be efficiently processed as compared to FE-based schemes where the creation of conforming discretisations for complex multiphase microstructures still poses a challenge.

As an application example consider the one-dimensional microscale boundary value problem depicted in Figure 2.13(a). The periodic microstructure, consisting of two different materials and the interphases between them, is subjected to the macroscale

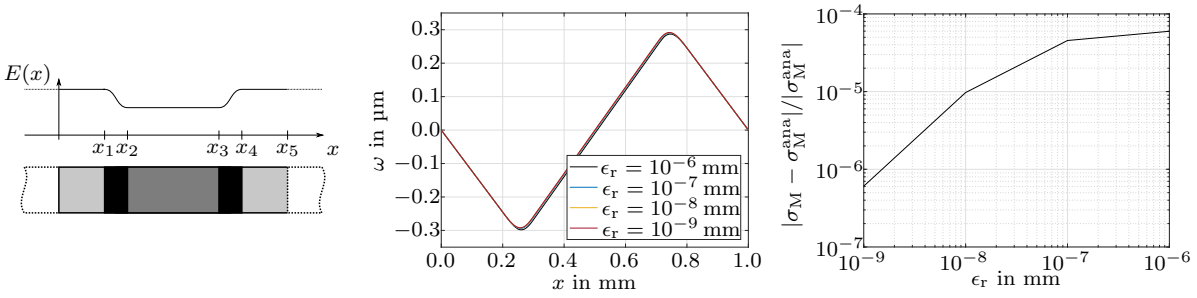

(a) boundary value problem (b) micro-fluctuation field (c) error in macroscale stresses

Figure 2.13: Periodic microstructure featuring material interphases: a) Sketch of microscale boundary value problem with periodic boundary conditions and spatially varying Young's modulus $E(x)$. b) Micro-fluctuation field $\omega(x)$ and c) relative error in predicted macroscale stress σ_{M} with respect to analytical solution $\sigma_{\mathrm{M}}^{\mathrm{ana}}$ for a prescribed macroscale strain state, $\varepsilon_{\mathrm{M}} = 0.005$, and various refinement tolerances ϵ_{r}. Simulation results for lifted interpolating wavelets ($N = 1$, $\tilde{N} = 1$, two-point forward differences) are shown. Reproduced from [45] under the terms of the Creative Commons Attribution 4.0 International License (CC BY 4.0).

strain ε_{M}. Moreover, a linear elastic material response is assumed with Young's modulus $E(x)$ being a function of space. For this setting, the micro-fluctuation field $\omega(x)$ that characterises the deviation from an affine deformation of the representative volume element and that represents the primary unknown of the proposed wavelet-collocation approach is depicted in Figure 2.13(b). Moreover, the convergence behaviour of the effective macroscale stress σ_{M} as a function of wavelet-refinement tolerance ϵ_{r} is exemplarily shown in Figure 2.13(c) for lifted-interpolating wavelets defined by the control parameters $N = 1$, $\tilde{N} = 1$. A decrease in refinement tolerance ϵ_{r} leads to the targeted activation of grid points on different resolution levels as shown in Figure 2.14. In particular, it is observed that grid points in the vicinity of the material interphases, i.e. in regions where significant changes in the solution profile are expected, are activated in the adaptive hierarchical wavelet approach.

The promising properties of wavelet-based approaches in the context of computational multiscale methods discussed in **Paper 6** motivate the development of a hybrid wavelet-FFT approach for the efficient solution of microscale boundary value problems in **Paper 7**.

2.4.2 Wavelet-enhanced FFT-based spectral solver

Motivated by the specific structure of the microscale boundary value problem, FFT-based solution approaches have been in the focus of intense research, see [27, 87] for detailed reviews. These approaches originate from the pioneering works [62, 72, 73] and rely on Fourier space representations of the governing fields and of the Eshelby-Green operator. Specifically speaking, the microscale boundary value problem is reformulated

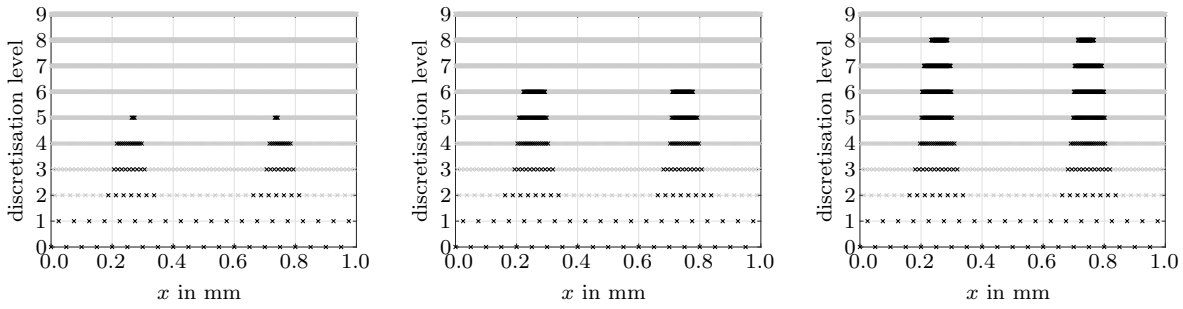

(a) $\epsilon_\mathrm{r} = 10^{-7}\,\mathrm{mm}$ (b) $\epsilon_\mathrm{r} = 10^{-8}\,\mathrm{mm}$ (c) $\epsilon_\mathrm{r} = 10^{-9}\,\mathrm{mm}$

Figure 2.14: Dyadic grids as a function of refinement tolerance ϵ_r for the microscale boundary value problem depicted in Figure 2.13(a) and a prescribed macroscale strain state, $\varepsilon_\mathrm{M} = 0.005$. The activation of grid points for lifted interpolating wavelets ($N = 1$, $\tilde{N} = 1$, two-point forward differences) is shown. Active grid points are indicated by black-coloured crosses, inactive grid points by grey-coloured crosses. Reproduced from [45] under the terms of the Creative Commons Attribution 4.0 International License (CC BY 4.0).

as an integral equation that can efficiently be evaluated in Fourier space and use is made of sophisticated implementations of the fast Fourier transform (FFT) [17, 25] to map field quantities from the physical to the frequency space and vice versa. Due to this reliance on efficient implementations of the FFT, a regular structured grid is assumed. This is a significant restriction when small-scale features occur in the solution domain since the grid spacing is determined by the smallest feature to be resolved. Thus, the system size and the number of material model evaluations significantly increase.

Against this background, a hybrid wavelet-FFT approach is developed in **Paper 7** that is based on adaptively refined computational grids such that localised features can be resolved accurately while the overall number of material model evaluations is significantly reduced. This is demonstrated by a detailed study of representative boundary value problems in one- and two-dimensional domains, with a reduction in the number of material model evaluations of up to 95% being achieved.

By introducing polarisation stresses $\boldsymbol{\tau}(\boldsymbol{x})$ that correspond to a reference material with stiffness tensor $\mathbf{E}^0$, the balance equation of linear momentum on the microscale domain $\mathcal{B}$ gives rise to the Lippmann-Schwinger-type equations for the strains

$$\widehat{\boldsymbol{\varepsilon}}(\boldsymbol{\xi}_\mathcal{B}) = -\widehat{\boldsymbol{\Gamma}^0}(\boldsymbol{\xi}_\mathcal{B}) : \widehat{\boldsymbol{\tau}}(\boldsymbol{\xi}_\mathcal{B}) \;\; \forall \; \boldsymbol{\xi}_\mathcal{B} \neq \mathbf{0} \quad , \quad \widehat{\boldsymbol{\varepsilon}}(\mathbf{0}) = \boldsymbol{\varepsilon}_\mathrm{M} \tag{2.22a}$$

$$\boldsymbol{\varepsilon}(\boldsymbol{x}) = -\boldsymbol{\Gamma}^0(\boldsymbol{\tau}(\boldsymbol{x})) + \boldsymbol{\varepsilon}_\mathrm{M} \;\; \forall \; \boldsymbol{x} \in \mathcal{B} \tag{2.22b}$$

where $\widehat{\bullet}$ indicates the Fourier coefficients of the field variable $\bullet$ at angular frequencies $\boldsymbol{\xi}_\mathcal{B}$. In Fourier space, representations of the Eshelby-Green operator $\widehat{\boldsymbol{\Gamma}^0}(\boldsymbol{\xi}_\mathcal{B})$ are available and its application reduces to tensor contractions. In particular, the specific form of the Eshelby-Green operator that is consistent with a discretisation in terms of Deslauriers-Dubuc wavelets [18] is derived in **Paper 7**.

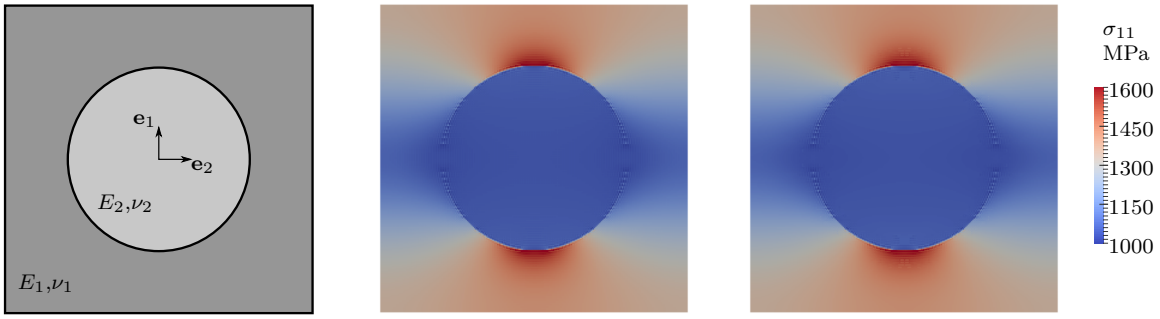

(a) matrix with soft inclusion (b) σ_{11}, non-adaptive (c) σ_{11}, $\epsilon_{\mathrm{W}} = 10^{-3}$

Figure 2.15: Hybrid wavelet-FFT approach for microscale boundary value problems: a) Matrix with soft inclusion. b) Stress distribution predicted by a non-adaptive and c) by an adaptive scheme for prescribed macroscale strains $\boldsymbol{\varepsilon}_{\mathrm{M}} = 0.005\,\mathbf{e}_1 \otimes \mathbf{e}_1$ and a linear elastic material response (Young's moduli: $E_2 = 0.6E_1$, Poisson's ratios: $\nu_1 = \nu_2$). Reproduced from [47] under the terms of the Creative Commons Attribution-NonCommercial-NoDerivatives 4.0 International License (CC BY-NC-ND 4.0).

In the light of the developments for fast and efficient FFT-based approaches the Barzilai-Borwein extended version of Moulinec-Suquet's basic scheme for the solution of (2.22) that was proposed in [86] is adopted. The scheme is based on the interpretation of the basic scheme as a gradient descent method and makes use of the well-established Barzilai-Borwein step size selection to be competitive with the fastest solvers available. More specifically speaking, the update scheme

$$ {}^{n+1}\boldsymbol{\varepsilon}\left(\boldsymbol{x}\right) = {}^{n}\boldsymbol{\varepsilon}\left(\boldsymbol{x}\right) - {}^{n}\gamma\left({}^{n}\boldsymbol{\sigma}\left(\boldsymbol{x}\right), {}^{n-1}\boldsymbol{\sigma}\left(\boldsymbol{x}\right), {}^{n-1}\gamma\right)\, \boldsymbol{\Gamma}^{0}\left({}^{n}\boldsymbol{\sigma}\left(\boldsymbol{x}\right)\right) \quad , \tag{2.23} $$

where counter n refers to the iteration step and with γ denoting the Barzilai-Borwein step size, is used. The evaluation of an update in strain space (2.23) requires the stress field ${}^{n}\boldsymbol{\sigma}\left(\boldsymbol{x}\right)$ to be determined for a given strain field ${}^{n}\boldsymbol{\varepsilon}\left(\boldsymbol{x}\right)$. For complex material behaviour this amounts to the numerical solution of a system of ordinary differential equations at each grid point, resulting in a significant computational effort. In this regard, the main idea of the approach proposed in **Paper 7** is to represent the stress field in a wavelet basis and to successively derive higher level stress approximations in the nested set of approximation spaces by making use of wavelet transforms. In doing so, localised microscale features can properly be resolved while a rather coarse discretisation is maintained in the remainder of the solution domain.

As an application example for the proposed adaptive hierarchical wavelet-FFT scheme, the unit cell featuring a matrix with a soft inclusion depicted in Figure 2.15(a) is considered. The unit cell is subjected to macroscale strains $\boldsymbol{\varepsilon}_{\mathrm{M}} = 0.005\,\mathbf{e}_1 \otimes \mathbf{e}_1$ and a linear elastic response of the individual constituents is assumed. The σ_{11} stress distribution that is predicted by a non-adaptive scheme based on a regular grid is shown in Figure 2.15(b) and the one predicted by the proposed adaptive scheme in Figure 2.15(c). Whereas

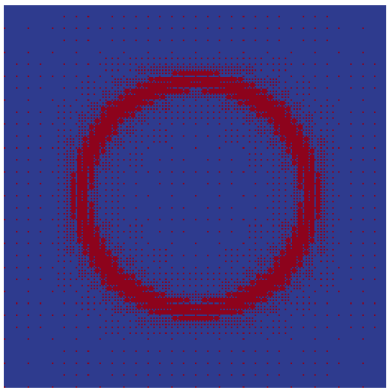

(a) iteration 0, $\epsilon_{\mathrm{W}} = 10^{-3}$

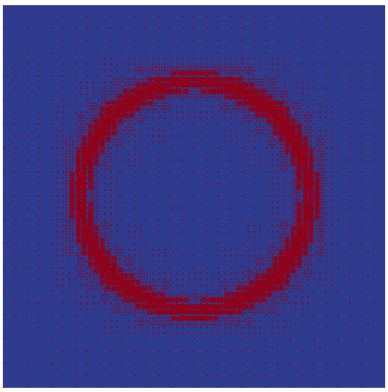

(b) iteration 0, $\epsilon_{\mathrm{W}} = 10^{-4}$

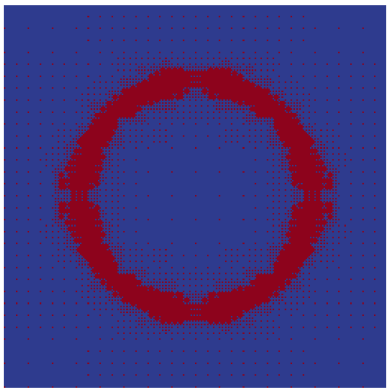

(c) iteration 2, $\epsilon_{\mathrm{W}} = 10^{-3}$

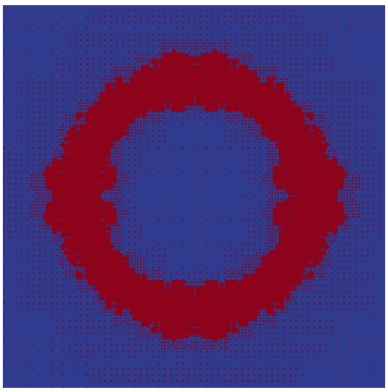

(d) iteration 2, $\epsilon_{\mathrm{W}} = 10^{-4}$

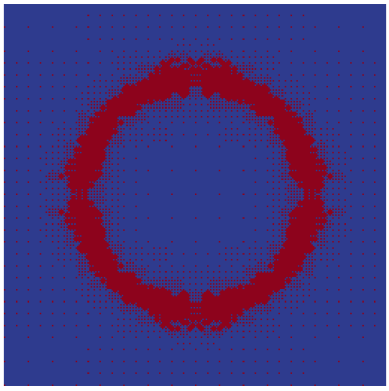

(e) iteration 4, $\epsilon_{\mathrm{W}} = 10^{-3}$

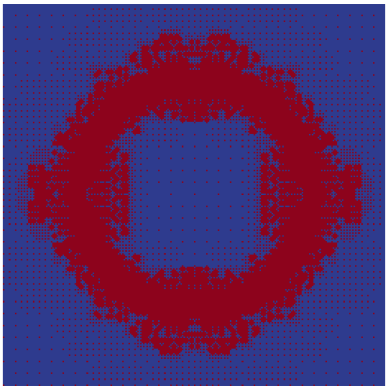

(f) iteration 4, $\epsilon_{\mathrm{W}} = 10^{-4}$

Figure 2.16: Activity of grid points in the tension problem of a unit cell with a soft inclusion depicted in Figure 2.15(a) for various iteration steps and values of refinement tolerance ϵ_{W}. The simulations are based on an Eshelby-Green operator associated with the wavelet discretisation. Active grid points are marked in red colour inactive grid points in blue colour. Reproduced from [47] under the terms of the Creative Commons Attribution-NonCommercial-NoDerivatives 4.0 International License (CC BY-NC-ND 4.0).

327680 material evaluations are required in the non-adaptive scheme, 52384 material evaluations are required in the adaptive scheme for a refinement tolerance $\epsilon_{\mathrm{W}} = 10^{-3}$ that controls the accuracy of the wavelet-based stress approximation. This significant gain is achieved by a targeted activation of grid points as exemplified in Figure 2.16 for different iterations.

As a different approach to account for microscale features in macroscopic stimulations, **Paper 8** focuses on the finite element implementation of a micromorphic continuum theory. In this regard, it is noted that the stress-gradient continuum approach under consideration can be motivated by means of an extended computational homogenisation scheme, cf. [34].

2.5 Stress gradient theory

Based on the works [24, 84, 96], **Paper 8** focuses on the development of a finite element implementation of the stress gradient theory as to study stress-free boundary layer and associated size effects. At the outset of the developments, a generalised (volume specific) stress energy density function of the form $w^*(\boldsymbol{\sigma}, \boldsymbol{R})$ in terms of the small deformation stress tensor $\boldsymbol{\sigma}$ and the third order hyperstress tensor $\boldsymbol{R}$ is postulated, and the stresses and hyperstresses are subjected to the extended set of static admissibility conditions

$$\nabla \cdot \boldsymbol{\sigma} = \boldsymbol{0} \quad , \tag{2.24a}$$

$$\boldsymbol{R} - [\nabla \boldsymbol{\sigma}]^{\mathrm{dev}} = \boldsymbol{0} \quad . \tag{2.24b}$$

By multiplying (2.24a) and (2.24b) with the kinematic field variables $\delta\boldsymbol{u}$ and $\delta\boldsymbol{\Phi}$, by integrating the ensuing equations over the domain $\mathcal{B}$ with boundary $\partial\mathcal{B}$ and with outward unit normal vector $\boldsymbol{n}$, and by applying the divergence theorem one arrives at

$$\underbrace{\int_{\mathcal{B}} \boldsymbol{\sigma} : [[\nabla \delta\boldsymbol{u}]^{\mathrm{sym}} + \nabla \cdot \delta\boldsymbol{\Phi}] + \boldsymbol{R} \therefore \delta\boldsymbol{\Phi} \, \mathrm{d}v}_{\mathcal{P}^{(i)}(\delta\boldsymbol{u}, \delta\boldsymbol{\Phi})} = \underbrace{\int_{\partial\mathcal{B}} \boldsymbol{\sigma} : [[\delta\boldsymbol{u} \otimes \boldsymbol{n}]^{\mathrm{sym}} + \delta\boldsymbol{\Phi} \cdot \boldsymbol{n}] \, \mathrm{d}a}_{\mathcal{P}^{(c)}(\delta\boldsymbol{u}, \delta\boldsymbol{\Phi})} \, . \tag{2.25}$$

Equation (2.25) can be interpreted as a generalised virtual work balance, with the virtual work of internal forces $\mathcal{P}^{(i)}(\delta\boldsymbol{u}, \delta\boldsymbol{\Phi})$ and the virtual work of contact forces $\mathcal{P}^{(c)}(\delta\boldsymbol{u}, \delta\boldsymbol{\Phi})$. With regard to the virtual work of internal forces $\mathcal{P}^{(i)}(\delta\boldsymbol{u}, \delta\boldsymbol{\Phi})$, energetic dualities are observed between the stresses $\boldsymbol{\sigma}$ and the generalised strain tensor

$$\boldsymbol{e} = [\nabla \boldsymbol{u}]^{\mathrm{sym}} + \nabla \cdot \boldsymbol{\Phi} \quad , \tag{2.26}$$

and between the hyperstress tensor $\boldsymbol{R}$ and the kinematic variable $\boldsymbol{\Phi}$, which is henceforth referred to as the micro-displacement tensor. The latter observation motivates the introduction of a generalised strain energy density function $w(\boldsymbol{e}, \boldsymbol{\Phi})$ such that

$$\boldsymbol{\sigma} = \frac{\partial w\left(\boldsymbol{e}, \boldsymbol{\Phi}\right)}{\partial \boldsymbol{e}} \quad , \qquad (2.27a) \qquad \boldsymbol{R} = \frac{\partial w\left(\boldsymbol{e}, \boldsymbol{\Phi}\right)}{\partial \boldsymbol{\Phi}} \quad . \qquad (2.27b)$$

By additionally introducing the generalised displacement field $\boldsymbol{\Psi} = \boldsymbol{\Psi}^{\mathrm{dev}} + \boldsymbol{\Psi}^{\mathrm{sph}}$, with

$$\boldsymbol{\Psi}^{\mathrm{dev}} = \boldsymbol{\Phi} \quad , \qquad (2.28a) \qquad \boldsymbol{\Psi}^{\mathrm{sph}} = \frac{1}{2}\left[\boldsymbol{u} \otimes \boldsymbol{I} + \boldsymbol{u} \mathbin{\overline{\otimes}} \boldsymbol{I}\right] \quad , \qquad (2.28b)$$

relation (2.25) can be recast in the form

$$\int_{\mathcal{B}} \boldsymbol{\sigma} : \left[\nabla \cdot \delta\boldsymbol{\Psi}\right] + \boldsymbol{R} \therefore \delta\boldsymbol{\Psi} \, \mathrm{d}v = \int_{\partial\mathcal{B}} \boldsymbol{\sigma} : \delta\boldsymbol{\Psi} \cdot \boldsymbol{n} \, \mathrm{d}a \quad . \qquad (2.29)$$

The virtual work statement (2.29) is particularly useful for the finite element implementation, as it implies that either the components of the stress tensor or the corresponding normal projections of the generalised displacement field can independently be prescribed. In this sense, the two-field problem in terms of the displacement field $\boldsymbol{u}$ and the micro-displacement field $\boldsymbol{\Phi}$ is reformulated in terms of one primary field quantity, i.e. in terms of the generalised displacement field $\boldsymbol{\Psi}$.

In the following, the symmetric positive definite quadratic form for the generalised stress energy density function

$$w^*\left(\boldsymbol{\sigma}, \boldsymbol{R}\right) = \frac{1}{2}\, \boldsymbol{\sigma} : \mathsf{C} : \boldsymbol{\sigma} + \frac{1}{2}\, \boldsymbol{R} \therefore \boldsymbol{\mathcal{C}} \therefore \boldsymbol{R} \quad , \qquad (2.30)$$

is assumed, with C and $\boldsymbol{\mathcal{C}}$ denoting the compliance and the generalised compliance tensor. By making use of the Legendre(-Fenchel) transform, the corresponding generalised strain energy density function takes the form

$$w\left(\boldsymbol{e}, \boldsymbol{\Phi}\right) = \frac{1}{2}\, \boldsymbol{e} : \mathsf{E} : \boldsymbol{e} + \frac{1}{2}\, \boldsymbol{\Phi} \therefore \boldsymbol{\mathcal{E}} \therefore \boldsymbol{\Phi} \quad , \qquad (2.31)$$

with the stiffness tensor E and the generalised stiffness tensor $\boldsymbol{\mathcal{E}}$ defined as $\mathsf{E} = \mathsf{C}^{-1}$ and $\boldsymbol{\mathcal{E}} = \boldsymbol{\mathcal{C}}^{-1}$. Moreover, a classic form for the stiffness tensor E in terms of the Lamé-type constants λ and μ, namely

$$\mathsf{E} = \lambda\, \boldsymbol{I} \otimes \boldsymbol{I} + 2\, \mu\, \mathsf{I}^{\mathrm{sym}} \quad , \qquad (2.32)$$

is adopted and the generalised stiffness tensor is assumed to take the form

$$\boldsymbol{\mathcal{E}} = \frac{\mu}{\ell^2}\, \boldsymbol{\mathcal{I}}^{\mathrm{sym,dev}} \quad , \qquad (2.33)$$

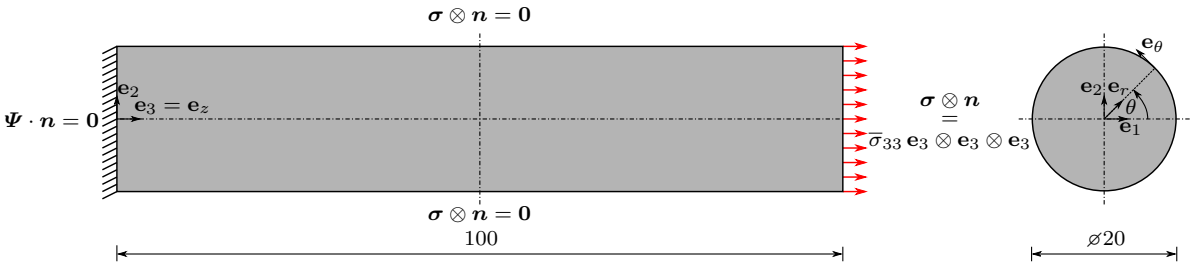

Figure 2.17: Geometric dimensions (in mm) and boundary conditions of the cylindrical bar under tension. Reproduced from [44] under the terms of the Creative Commons Attribution 4.0 International License (CC BY 4.0).

with $\mathsf{I}^{\mathrm{sym}}$ and $\boldsymbol{\mathcal{I}}^{\mathrm{sym,dev}}$ denoting the fourth order symmetric and the sixth order symmetric and deviatoric projection tensors. As opposed to classic strain gradient approaches, it is observed that the length scale parameter ℓ naturally occurs in the denominator, indicating a smaller-is-softer-type size effect.

The virtual work statement (2.29) and the specific form of the generalised stiffness tensor (2.33) stipulate two salient features of the stress gradient theory: a generalised Neumann boundary condition that allows for the (complete) stress tensor to be prescribed in simulations and the occurrence of a smaller-is-softer-type size effect. To demonstrate these, focus is laid on the cylindrical bar depicted in Figure 2.17. At the left boundary ($z = 0\,\mathrm{mm}$), generalised clamping boundary conditions of the form $\boldsymbol{\Psi} \cdot \boldsymbol{n} = \mathbf{0}$ are assumed for the generalised displacement field. At the right boundary ($z = 100\,\mathrm{mm}$), generalised traction boundary conditions of the form

$$\boldsymbol{\sigma} \otimes \boldsymbol{n} = \overline{\sigma}_{33}\, \mathbf{e}_3 \otimes \mathbf{e}_3 \otimes \mathbf{e}_3 \quad , \tag{2.34}$$

with the overbar indicating a prescribed quantity, are applied. Moreover, the outer surface of the cylindrical bar ($r = 10\,\mathrm{mm}$) is assumed to be stress-free, i.e.

$$\boldsymbol{\sigma} \otimes \boldsymbol{n} = \boldsymbol{\sigma} \otimes \mathbf{e}_r = \mathbf{0} \quad . \tag{2.35}$$

First, it is observed that the boundary condition (2.35) causes all coefficients of the stress tensor to approach zero at the lateral surface. This is a significant difference compared to the classic Cauchy continuum approach where only the normal projection of the stress tensor can be prescribed and where a constant stress profile $\sigma_{zz} \approx 2100\,\mathrm{N\,mm^{-2}}$ is expected for the given boundary value problem when an isotropic, linear elastic material response is assumed. In contrast, σ_{zz} takes a parabolic profile in the present case, with the extreme value at $r = 0\,\mathrm{mm}$ and the slope of the profile being functions of the material length scale parameter ℓ, see Figures 2.18(a) and 2.19(a). The in-plane coefficients of the stress tensor σ_{rr} and σ_{zz}, which would take zero values for a classic Cauchy continuum theory, are depicted in Figures 2.18(b) and 2.18(c). They are observed to be approx. two orders of magnitude smaller than the axial stresses and to approach zero at the lateral surface of the bar due to the vanishing stress boundary conditions.

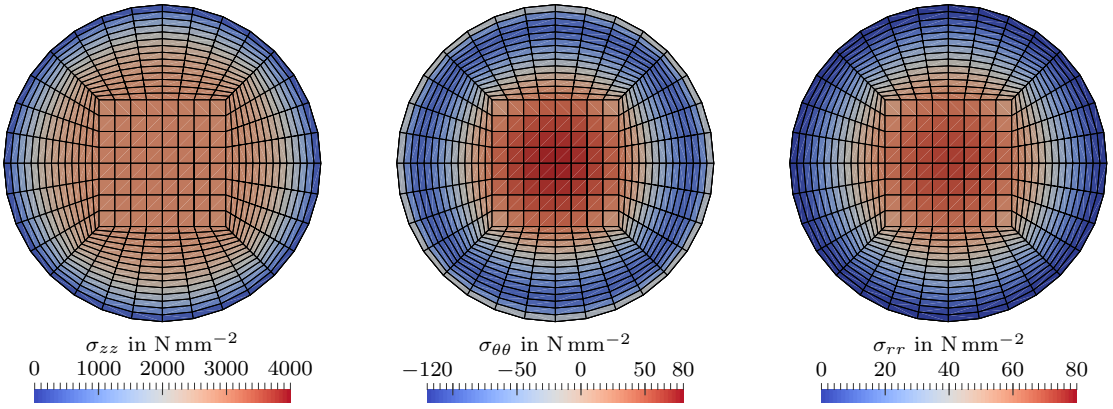

(a) axial stress (b) circumferential stress (c) radial stress

Figure 2.18: Stress distribution predicted by finite element calculations of the tensile problem depicted in Figure 2.17 ($E = 210\,000\,\mathrm{N/mm^2}, \nu = 0.3, \ell = 1.0\,\mathrm{mm}$). Reproduced from [44] under the terms of the Creative Commons Attribution 4.0 International License (CC BY 4.0).

In addition to the finite element simulation results, an analytical solution is provided in Figure 2.19(a) for validation purposes and the axial stiffness $\mathcal{K}_\ell$ and torsional stiffness $\mathcal{J}_\ell$, normalised with respect to a classic Cauchy continuum, are provided in Figure 2.19(b) as functions of the characteristic length scale ratio. Whereas the stiffness of a classic Cauchy continuum is recovered in the limit of an infinite length scale ratio, boundary layer effects become dominant with decreasing length scale ratio and a smaller-is-softer-type size effect is observed.

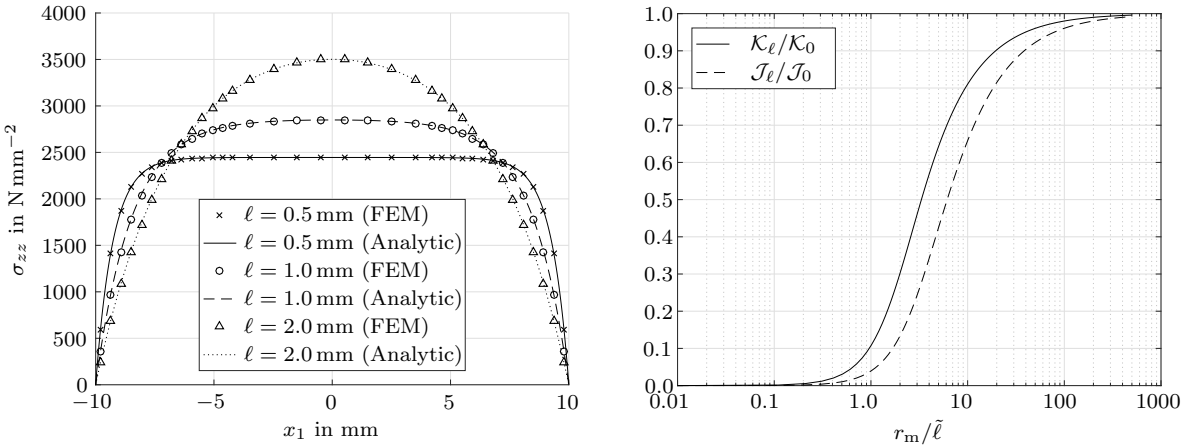

(a) validation and boundary layer effects (b) circumferential stress

Figure 2.19: Validation of the finite element implementation of the stress gradient theory and a study of boundary layer and associated size effects: a) Finite element and analytic solution of the simple tensile problem depicted in Figure 2.17 ($E = 210\,000\,\mathrm{N/mm^2}, \nu = 0$). b) Relative stiffness of a cylindrical bar in tension and in torsion as a function of the ratio between the bar radius r_m and the intrinsic length scale $\tilde{\ell} = \sqrt{2}\,\ell$. Reproduced from [44] under the terms of the Creative Commons Attribution 4.0 International License (CC BY 4.0).

3 Concluding remarks

A brief summary of the main contributions (**C-RQ**) in relation to the research questions (**RQ**) posed in Section 1.2 is provided in this section:

C-RQ 1: A computational multiscale approach for electrical conductors in an infinitesimal deformation setting was developed and a FE^2-based implementation was discussed. In particular, it was shown that the proposed approach enables the calculation of effective conductivity tensors for given, possibly evolving, microstructures.

C-RQ 2: A computational multiscale approach for electrical conductors in a finite deformation setting was developed and a FE^2-based implementation was discussed. In particular, it was shown that the influence of finite geometry changes, e.g. of microscale pores, on the effective conductivity can be accounted for in the proposed finite deformation multiscale approach.

C-RQ 3: It was shown that experimentally recorded changes in conductivity caused by the presence of geometrically well-defined microscale pores can be accounted for in simulations by making use of the proposed computational multiscale approach. Moreover, a sensitivity analysis of the experimental data was carried out and the usefulness of the proposed modelling approach to interpret experimental data was demonstrated.

C-RQ 4: It was shown that experimentally recorded changes in the conductivity of cyclically strained metal thin films can, in principle, be related to microscale cracks by automated generation and processing of unit cells based on CLSM laser intensity images. However, the study also revealed severe challenges with regard to the interpretation of the CLSM images and the generation of unit cells based thereof.

C-RQ 5: An electro-mechanically coupled cohesive zone formulation for electrical conductors was developed and a finite element-based implementation was proposed. The formulation allows for the possibly evolving electrical resistivity of material interfaces, for instance caused by mechanically-induced degradation processes, to be considered in simulations.

C-RQ 6: A wavelet collocation approach for the solution of microscale boundary value problems was developed, and fundamental features such as adaptivity and

grid refinement capabilities, mapping algorithms for internal variables and (discrete) scale-bridging relations were investigated.

C-RQ 7: An adaptive hierarchical wavelet-enhanced FFT-based approach for the efficient solution of microscale boundary value problems was developed and the corresponding Eshelby-Green operator associated with the underlying wavelet discretisation was derived. A significant reduction in the number of material model evaluations as compared to a non-adaptive approach was achieved with the novel wavelet-FFT-approach.

C-RQ 8: A finite element implementation of the stress-gradient theory was developed and analytical solutions were derived for validation purposes. Furthermore, it was shown that the formulation allows for stress-free boundary layer effects and smaller-is-softer-type size effects to be accounted for in simulations.

and future research directions (**D-RQ**) emanating from **Paper 1**–**Paper 8** are discussed:

D-RQ 1,2: The computational homogenisation approach developed in **Paper 1** and **Paper 2** relies on accurate representations of the underlying material microstructure and on appropriate microscale material models. This includes microscale features such as material interfaces and evolving microscale cracks that can be accounted for in (single-scale) simulations by using the cohesive zone approach developed in **Paper 5**. Against this background, the developed computational multiscale approach is to be extended as to account for unit cells featuring material interfaces. Moreover, the evolution of microscale cracks may induce softening at the macroscale such that appropriate regularisation approaches need to be developed. Furthermore, it is natural to additionally consider thermal coupling in future works since the flow of electric charge is intrinsically dissipative.

D-RQ 3: The detailed understanding of the influence of microscale pores on the effective electrical conductivity gained in **Paper 3** is to be complemented by further experimental and simulation-based studies focusing, for instance, on the dislocation density and on grain and phase boundaries. With such a systematically developed modelling approach at hand, the individual contributions of different microscale features to the overall resistivity of a sample may be distinguished and predictive simulation approaches may be developed.

D-RQ 4: In accordance with the experimental determination of crack densities, the identification of cracks and the associated generation of unit cells in **Paper 4** were based on the grey scale gradient of laser intensity images. The procedure was observed to be sensitive with regard to the particular choice of a filter parameter. Moreover, the non-trivial distinction between plastic localisation zones and through thickness cracks, and the identification of crack patterns

in the case of weakly pronounced grey scale gradients pose severe challenges. Against this background, further combined numerical and experimental studies are required.

D-RQ 5: The electro-mechanically coupled cohesive zone formulation developed in **Paper 5** makes it possible to account for the influence of material interfaces at different length scales. Focusing on the microscale, experimental data for grain and phase boundaries is to be taken into account in a next step to calibrate the generalised traction-separation laws. Focusing on the macroscale, computational homogenisation schemes for material interfaces are promising approaches to account for the underlying material microstructure when developing generalised traction-separations laws for electro-mechanically coupled problems.

D-RQ 6,7: Fundamental properties of wavelet-based approaches when applied to multiscale problems in continuum mechanics were studied in **Paper 6**, and a hybrid wavelet-FFT approach for the efficient solution of microscale boundary value problems was developed in **Paper 7**. The numerical performance of the hybrid approach was studied in a simplified setting, adopting linear elastic constitutive relations. However, an even more significant gain in computational efficiency is expected when applied to materials exhibiting nonlinear history-dependent behaviour since these require, in general, a system of evolution equations to be solved at quadrature point level. Being based on adaptive irregular grids, such a study requires mapping algorithms for internal variables such as the wavelet-based ones developed in **Paper 6**.

D-RQ 8: Stress-free boundary layer and associated smaller-is-softer-type size effects have been reported in experiments on metallic foams as summarised in Section 1.1.4. Against this background and with the developments of **Paper 8** at hand, the question naturally arises if the experimental findings can be reproduced by using a stress gradient continuum theory at the macroscale.

Bibliography

[1] K. Amaratunga and J. R. Williams. Wavelet based Green's function approach to 2D PDEs. *Engineering Computations*, 10:349–367, 1993. doi:10.1108/eb023913.

[2] K. Amaratunga, J. R. Williams, S. Qian, and J. Weiss. Wavelet-Galerkin solutions for one-dimensional partial differential equations. *International Journal for Numerical Methods in Engineering*, 37(16):2703–2716, 1994. doi:10.1002/nme.1620371602.

[3] E. W. Andrews, G. Gioux, P. Onck, and L. J. Gibson. Size effects in ductile cellular solids. Part II: experimental results. *International Journal of Mechanical Sciences*, 43(3):701–713, 2001. doi:10.1016/S0020-7403(00)00043-6.

[4] I. Arias, S. Serebrinsky, and M. Ortiz. A phenomenological cohesive model of ferroelectric fatigue. *Acta Materialia*, 54(4):975–984, 2006. doi:10.1016/j.actamat.2005.10.035.

[5] F. Axisa, P. M. Schmitt, C. Gehin, G. Delhomme, E. McAdams, and A. Dittmar. Flexible technologies and smart clothing for citizen medicine, home healthcare, and disease prevention. *IEEE Transactions on Information Technology in Biomedicine*, 9(3):325–336, 2005. doi:10.1109/TITB.2005.854505.

[6] Y. Azdoud and S. Ghosh. Adaptive wavelet-enriched hierarchical finite element model for polycrystalline microstructures. *Computer Methods in Applied Mechanics and Engineering*, 370:337–360, 2017. doi:10.1016/j.cma.2017.04.018.

[7] Y. Azdoud, J. Cheng, and S. Ghosh. Wavelet-enriched adaptive crystal plasticity finite element model for polycrystalline microstructures. *Computer Methods in Applied Mechanics and Engineering*, 327:36–57, 2017. doi:10.1016/j.cma.2017.08.026.

[8] G. I. Barenblatt. The formation of equilibrium cracks during brittle fracture. General ideas and hypotheses. Axially-symmetric cracks. *Journal of Applied Mathematics and Mechanics*, 23(3):622–636, 1959. doi:10.1016/0021-8928(59)90157-1.

[9] S. Bargmann, B. Klusemann, J. Markmann, J. E. Schnabel, K. Schneider, C. Soyarslan, and J. Wilmers. Generation of 3D representative volume elements for heterogeneous materials: A review. *Progress in Materials Science*, 96:322–384, 2018. doi:10.1016/j.pmatsci.2018.02.003.

[10] R. Berthelsen and A. Menzel. Computational homogenisation of thermo-viscoplastic composites: Large strain formulation and weak micro-periodicity. *Computer Methods in Applied Mechanics and Engineering*, 348:575–603, 2019. doi:10.1016/j.cma.2018.12.032.

[11] R. Berthelsen, R. Denzer, P. Oppermann, and A. Menzel. Computational homogenisation for thermoviscoplasticity: Application to thermally sprayed coatings. *Computational Mechanics*, 60(5):739–766, 2017. doi:10.1007/s00466-017-1436-x.

[12] Y. Chen, J. Au, P. Kazlas, A. Ritenour, H. Gates, and M. McCreary. Flexible active-matrix electronic ink display. *Nature*, 423(6936):136, 2003. doi:10.1038/423136a.

[13] M. A. Christon and D. W. Roach. The numerical performance of wavelets for PDEs: the multi-scale finite element. *Computational Mechanics*, 25:230–244, 2000. doi:10.1007/s004660050472.

[14] E. W. C. Coenen, V. G. Kouznetsova, E. Bosco, and M. G. D. Geers. A multi-scale approach to bridge microscale damage and macroscale failure: a nested computational homogenization-localization framework. *International Journal of Fracture*, 178:157–178, 2012. doi:10.1007/s10704-012-9765-4.

[15] E. W. C. Coenen, V. G. Kouznetsova, and M. G. D. Geers. Multi-scale continuous-discontinuous framework for computational-homogenization-localization. *Journal of the Mechanics and Physics of Solids*, 60(8):1486–1507, 2012. doi:10.1088/0965-0393/19/7/074008.

[16] M. J. Cordill, O. Glushko, J. Kreith, V. M. Marx, and C. Kirchlechner. Measuring electro-mechanical properties of thin films on polymer substrates. *Microelectronic Engineering*, 137:96–100, 2015. doi:10.1016/j.mee.2014.08.002.

[17] L. Dalcin, M. Mortensen, and D. E. Keyes. Fast parallel multidimensional FFT using advanced MPI. *Journal of Parallel and Distributed Computing*, 128:137–150, 2019. doi:10.1016/j.jpdc.2019.02.006.

[18] G. Deslauriers and S. Dubuc. Symmetric iterative interpolation processes. *Constructive Approximation*, 5:49–68, 1989. doi:10.1007/978-1-4899-6886-9_3.

[19] D. S. Dugdale. Yielding of steel sheets containing slits. *Journal of the Mechanics and Physics of Solids*, 8(2):100–104, 1960. doi:10.1016/0022-5096(60)90013-2.

[20] M. Erinc, P. J. G. Schreurs, and M. G. D. Geers. Integrated numerical-experimental analysis of interfacial fatigue fracture in SnAgCu solder joints. *International Journal of Solids and Structures*, 44(17):5680–5694, 2007. doi:10.1016/j.ijsolstr.2007.01.021.

[21] A. Esmaeili, A. Javili, and P. Steinmann. A thermo-mechanical cohesive zone model accounting for mechanically energetic Kapitza interfaces. *International Journal of Solids and Structures*, 92–93:29–44, 2016. doi:10.1016/j.ijsolstr.2016.04.035.

[22] M. Fagerström and R. Larsson. A thermo-mechanical cohesive zone formulation for ductile fracture. *Journal of the Mechanics and Physics of Solids*, 56(10):3037–3058, 2008. doi:10.1016/j.jmps.2008.06.002.

[23] Y. F. Fangye, N. Miska, and D. Balzani. Automated simulation of voxel-based microstructures based on enhanced finite cell approach. *Archive of Applied Mechanics*, 90:2255–2273, 2020. doi:10.1007/s00419-020-01719-x.

[24] S. Forest and K. Sab. Stress gradient continuum theory. *Mechanics Research Communications*, 40:16–25, 2012. doi:10.1016/j.mechrescom.2011.12.002.

[25] M. Frigo and S. Johnson. The design and implementation of FFTW3. *Proceedings of the IEEE*, 93(2):216–231, 2005. doi:10.1109/JPROC.2004.840301.

[26] M. G. D. Geers, V. G. Kouznetsova, and W. A. M. Brekelmans. Multi-scale computational homogenization: Trends and challenges. *Journal of Computational and Applied Mathematics*, 234(7):2175–2182, 2010. doi:10.1016/j.cam.2009.08.077.

[27] C. Gierden, J. Kochmann, J. Waimann, B. Svendsen, and S. Reese. A review of FE-FFT-based two-scale methods for computational modeling of microstructure evolution and macroscopic material behavior. *Archives of Computational Methods in Engineering*, 29:4115–4135, 2022. doi:10.1007/s11831-022-09735-6.

[28] O. Glushko, A. Klug, E. J. List-Kratochvil, and M. J. Cordill. Monotonic and cyclic mechanical reliability of metallization lines on polymer substrates. *Journal of Materials Research*, 32(9):1760–1769, 2017. doi:10.1557/jmr.2017.121.

[29] A. Grossmann, J. Morlet, and T. Paul. Transforms associated to square integrable group representations. I. General results. *Journal of Mathematical Physics*, 26(10): 2473–2479, 1985. doi:10.1063/1.526761.

[30] M. E. Gurtin and A. I. Murdoch. A continuum theory of elastic material surfaces. *Archive for Rational Mechanics and Analysis*, 57(4):291–323, 1975. doi:10.1007/BF00261375.

[31] C. Harnish, K. Matouš, and D. Livescu. Adaptive wavelet algorithm for solving nonlinear initial-boundary value problems with error control. *International Journal for Multiscale Computational Engineering*, 16(1):19–43, 2018. doi:10.1615/IntJMultCompEng.2018024915.

[32] C. Harnish, L. Dalessandro, K. Matouš, and D. Livescu. A multiresolution adaptive wavelet method for nonlinear partial differential equations. *International Journal for Multiscale Computational Engineering*, 19(2):29–37, 2021. doi:10.1615/IntJMultCompEng.2021039451.

[33] T. Heitbreder, N. S. Ottosen, M. Ristinmaa, and J. Mosler. Consistent elastoplastic cohesive zone model at finite deformations – Variational formulation. *International Journal of Solids and Structures*, 106–107:284–293, 2017. doi:10.1016/j.ijsolstr.2016.10.027.

[34] G. Hütter, K. Sab, and S. Forest. Kinematics and constitutive relations in the stress–gradient theory: Interpretation by homogenization. *International Journal of Solids and Structures*, 193–194:90–97, 2020. doi:10.1016/j.ijsolstr.2020.02.014.

[35] R. Jänicke and H. Steeb. Minimal loading conditions for higher-order numerical homogenisation schemes. *Archive of Applied Mechanics*, 82(8):1075–1088, 2012. doi:10.1007/s00419-012-0614-8.

[36] A. Javili, G. Chatzigeorgiou, and P. Steinmann. Computational homogenization in magneto-mechanics. *International Journal of Solids and Structures*, 50(25): 4197–4216, 2013. doi:10.1016/j.ijsolstr.2013.08.024.

[37] A. Javili. Variational formulation of generalized interfaces for finite deformation elasticity. *Mathematics and Mechanics of Solids*, 23(9):1303–1322, 2018. doi:10.1177/1081286517719938.

[38] A. Javili, P. Steinmann, and J. Mosler. Micro-to-macro transition accounting for general imperfect interfaces. *Computer Methods in Applied Mechanics and Engineering*, 317:274–317, 2017. doi:10.1016/j.cma.2016.12.025.

[39] S. Jones and M. Legrand. The wavelet-Galerkin method for solving PDE's with spatially de-pendent variables. *19th International Congress on Sound and Vibration (ICSV19)*, pages 1–8, 2012.

[40] T. Kaiser and A. Menzel. Fundamentals of electro-mechanically coupled cohesive zone formulations for electrical conductors. *Computational Mechanics*, 68(1):51–67, 2021. doi:10.1007/s00466-021-02019-z.

[41] T. Kaiser, M. J. Cordill, C. Kirchlechner, and A. Menzel. Electrical and mechanical behaviour of metal thin films with deformation-induced cracks predicted by computational homogenisation. *International Journal of Fracture*, 231(2):223–242, 2021. doi:10.1007/s10704-021-00582-3.

[42] T. Kaiser and A. Menzel. An electro-mechanically coupled computational multiscale formulation for electrical conductors. *Archive of Applied Mechanics*, 91: 1509–1526, 2021. doi:10.1007/s00419-020-01837-6.

[43] T. Kaiser and A. Menzel. A finite deformation electro-mechanically coupled computational multiscale formulation for electrical conductors. *Acta Mechanica*, 232: 3939–3956, 2021. doi:10.1007/s00707-021-03005-5.

[44] T. Kaiser, S. Forest, and A. Menzel. A finite element implementation of the stress gradient theory. *Meccanica*, 56(5):1109–1128, 2021. doi:10.1007/s11012-020-01266-3.

[45] T. Kaiser, J. J. C. Remmers, and M. G. D. Geers. An adaptive wavelet-based collocation method for solving multiscale problems in continuum mechanics. *Computational Mechanics*, 70:1335–1357, 2022. doi:10.1007/s00466-022-02207-5.

[46] T. Kaiser, G. Dehm, C. Kirchlechner, A. Menzel, and H. Bishara. Probing porosity in metals by electrical conductivity: Nanoscale experiments and multiscale simulations. *European Journal of Mechanics – A/Solids*, 97:104777, 2023. doi:10.1016/j.euromechsol.2022.104777.

[47] T. Kaiser, T. Raasch, J. J. C. Remmers, and M. G. D. Geers. A wavelet-enhanced adaptive hierarchical FFT-based approach for the efficient solution of microscale boundary value problems. *Computer Methodsin Applied Mechanics and Engineer-*

ing, 409:115959, 2023. doi:10.1016/j.cma.2023.115959.

[48] M.-A. Keip, P. Steinmann, and J. Schröder. Two-scale computational homogenization of electro-elasticity at finite strains. *Computer Methods in Applied Mechanics and Engineering*, 278:62–79, 2014. doi:10.1016/j.cma.2014.04.020.

[49] M. Khalaquzzaman, B.-X. Xu, S. Ricker, and R. Müller. Computational homogenization of piezoelectric materials using FE2 to determine configurational forces. *Technische Mechanik*, 32(1):21–37, 2012.

[50] J. E. Kim, G.-W. Jang, and Y. Y. Kim. Adaptive multiscale wavelet-Galerkin analysis for plane elasticity problems and its applications to multiscale topology design optimization. *International Journal of Solids and Structures*, 40(23):6473–6496, 2003. doi:10.1016/S0020-7683(03)00417-7.

[51] S. Kim, H.-J. Kwon, S. Lee, H. Shim, Y. Chun, W. Choi, J. Kwack, D. Han, M. Song, S. Kim, S. Mohammadi, I. Kee, and S. Y. Lee. Low-power flexible organic light-emitting diode display device. *Advanced Materials*, 23(31):3511–3516, 2011. doi:10.1002/adma.201101066.

[52] A. Koch, M. Bonhage, M. Teschke, L. Lücker, B.-A. Behrens, and F. Walther. Electrical resistance-based fatigue assessment and capability prediction of extrudates from recycled field-assisted sintered EN AW-6082 aluminium chips. *Materials Characterization*, 169:110644, 2020. doi:10.1016/j.matchar.2020.110644.

[53] V. G. Kouznetsova, W. A. M. Brekelmans, and F. P. T. Baaijens. An approach to micro-macro modeling of heterogeneous materials. *Computational Mechanics*, 27 (1):37–48, 2001. doi:10.1007/s004660000212.

[54] V. G. Kouznetsova, M. G. D. Geers, and W. A. M. Brekelmans. Multi-scale constitutive modelling of heterogeneous materials with a gradient-enhanced computational homogenization scheme. *International Journal for Numerical Methods in Engineering*, 54(8):1235–1260, 2002. doi:10.1002/nme.541.

[55] V. G. Kouznetsova, M. G. D. Geers, and W. A. M. Brekelmans. Multi-scale second-order computational homogenization of multi-phase materials: a nested finite element solution strategy. *Computer Methods in Applied Mechanics and Engineering*, 193(48):5525–5550, 2004. doi:10.1016/j.cma.2003.12.073.

[56] S. Kozinov and M. Kuna. Simulation of damage in ferroelectric actuators by means of cohesive zone model. *Sensors and Actuators A: Physical*, 233:176–183, 2015. doi:10.1016/j.sna.2015.06.030.

[57] S. Kozinov, M. Kuna, and S. Roth. A cohesive zone model for the electromechanical damage of piezoelectric/ferroelectric materials. *Smart Materials and Structures*, 23(5):055024, 2014. doi:10.1088/0964-1726/23/5/055024.

[58] P. Kreiml, M. Rausch, V. L. Terziyska, H. Köstenbauer, J. Winkler, C. Mitterer, and M. J. Cordill. Correlation of mechanical damage and electrical behavior

of Al/Mo bilayers subjected to bending. *Thin Solid Films*, 687:137480, 2019. doi:10.1016/j.tsf.2019.137480.

[59] B. Li and X. Chen. Wavelet-based numerical analysis: A review and classification. *Finite Elements in Analysis and Design*, 81:14–31, 2014. doi:10.1016/j.finel.2013.11.001.

[60] S. G. Mallat. A theory for multiresolution signal decomposition: the wavelet representation. *IEEE Transactions on Pattern Analysis and Machine Intelligence*, 11(7):674–693, 1989. doi:10.1109/34.192463.

[61] K. Matouš, M. G. D. Geers, V. G. Kouznetsova, and A. Gillman. A review of predictive nonlinear theories for multiscale modeling of heterogeneous materials. *Journal of Computational Physics*, 330:192–220, 2017. doi:10.1016/j.jcp.2016.10.070.

[62] J. C. Michel, H. Moulinec, and P. Suquet. Effective properties of composite materials with periodic microstructure: a computational approach. *Computer Methods in Applied Mechanics and Engineering*, 172(1):109–143, 1999. doi:10.1016/S0045-7825(98)00227-8.

[63] C. Miehe, J. Schröder, and C. Bayreuther. On the homogenization analysis of composite materials based on discretized fluctuations on the micro-structure. *Acta Mechanica*, 155(1-2):1–16, 2002. doi:10.1007/BF01170836.

[64] C. Miehe and A. Koch. Computational micro-to-macro transitions of discretized microstructures undergoing small strains. *Archive of Applied Mechanics*, 72(4-5): 300–317, 2002. doi:10.1007/s00419-002-0212-2.

[65] C. Miehe, J. Schotte, and J. Schröder. Computational micro-macro transitions and overall moduli in the analysis of polycrystals at large strains. *Computational Materials Science*, 16(1):372–382, 1999. doi:10.1016/S0927-0256(99)00080-4.

[66] C. Miehe, J. Schröder, and J. Schotte. Computational homogenization analysis in finite plasticity. Simulation of texture development in polycrystalline materials. *Computer Methods in Applied Mechanics and Engineering*, 171(3):387–418, 1999. doi:10.1016/S0045-7825(98)00218-7.

[67] R. D. Mindlin. Second gradient of strain and surface-tension in linear elasticity. *International Journal of Solids and Structures*, 1(4):417–438, 1965. doi:10.1016/0020-7683(65)90006-5.

[68] R. D. Mindlin and N. N. Eshel. On first strain gradient theories in linear elasticity. *International Journal of Solids Structures*, 4(1):109–124, 1968. doi:10.1016/0020-7683(68)90036-X.

[69] K. Mitsubayashi, Y. Wakabayashi, D. Murotomi, T. Yamada, T. Kawase, S. Iwagaki, and I. Karube. Wearable and flexible oxygen sensor for transcutaneous oxygen monitoring. *Sensors and Actuators B: Chemical*, 95(1):373–377, 2003. doi:10.1016/S0925-4005(03)00441-6.

[70] J. Morlet, G. Arens, E. Fourgeau, and D. Glard. Wave propagation and sampling theory–Part I: Complex signal and scattering in multilayered media. *Geophysics*, 47(4):203–221, 1982. doi:10.1190/1.1441328.

[71] J. Mosler and I. Scheider. A thermodynamically and variationally consistent class of damage-type cohesive models. *Journal of the Mechanics and Physics of Solids*, 59(8):1647–1668, 2011. doi:10.1016/j.jmps.2011.04.012.

[72] H. Moulinec and P. Suquet. A fast numerical method for computing the linear and nonlinear mechanical properties of composites. *Comptes rendus de l'Académie des sciences. Série II, Mécanique, physique, chimie, astronomie*, 318(11):1417–1426, 1994.

[73] H. Moulinec and P. Suquet. A numerical method for computing the overall response of nonlinear composites with complex microstructure. *Computer Methods in Applied Mechanics and Engineering*, 157(1):69–94, 1998. doi:10.1016/S0045-7825(97)00218-1.

[74] A. I. Murdoch. A thermodynamical theory of elastic material interfaces. *The Quarterly Journal of Mechanics and Applied Mathematics*, 29(3):245–275, 1976. doi:10.1093/qjmam/29.3.245.

[75] P. R. Onck, E. W. Andrews, and L. J. Gibson. Size effects in ductile cellular solids. Part I: modeling. *International Journal of Mechanical Sciences*, 43(3):681–699, 2001. ISSN 0020-7403. doi:10.1016/S0020-7403(00)00042-4.

[76] M. Ostoja-Starzewski. Macrohomogeneity condition in dynamics of micropolar media. *Archive of Applied Mechanics*, 81(7):899–906, 2011. doi:10.1007/s00419-010-0456-1.

[77] N. S. Ottosen and M. Ristinmaa. Thermodynamically based fictitious crack/interface model for general normal and shear loading. *International Journal of Solids and Structures*, 50(22):3555–3561, 2013. doi:10.1016/j.ijsolstr.2013.06.019.

[78] N. S. Ottosen, M. Ristinmaa, and J. Mosler. Fundamental physical principles and cohesive zone models at finite displacements – limitations and possibilities. *International Journal of Solids and Structures*, 53:70–79, 2015. doi:10.1016/j.ijsolstr.2014.10.020.

[79] N. S. Ottosen, M. Ristinmaa, and J. Mosler. Framework for non-coherent interface models at finite displacement jumps and finite strains. *Journal of the Mechanics and Physics of Solids*, 90:124–141, 2016. doi:10.1016/j.jmps.2016.02.034.

[80] I. Özdemir, W. A. M. Brekelmans, and M. G. D. Geers. FE^2 computational homogenization for the thermo-mechanical analysis of heterogeneous solids. *Computer Methods in Applied Mechanics and Engineering*, 198(3):602–613, 2008. doi:10.1016/j.cma.2008.09.008.

[81] I. Özdemir, W. A. M. Brekelmans, and M. G. D. Geers. A thermo-mechanical cohesive zone model. *Computational Mechanics*, 46(5):735–745, 2010. doi:10.1007/s00466-010-0507-z.

[82] J. Renard and M. F. Marmonier. Etude de l'initiation de l'endommagement dans la matrice d'un matériau composite par une méthode d'homogénéisation. *Aerospace Science and Technology*, (6):43–51, 1987.

[83] P. Robinson, U. Galvanetto, D. Tumino, G. Bellucci, and D. Violeau. Numerical simulation of fatigue-driven delamination using interface elements. *International Journal for Numerical Methods in Engineering*, 63(13):1824–1848, 2005. doi:10.1002/nme.1338.

[84] K. Sab, F. Legoll, and S. Forest. Stress gradient elasticity theory: Existence and uniqueness of solution. *Journal of Elasticity*, 123(2):179–201, 2016. doi:10.1007/s10659-015-9554-1.

[85] S. Saeb, P. Steinmann, and A. Javili. On effective behavior of microstructures embedding general interfaces with damage. *Computational Mechanics*, 64(6):1473–1494, 2019. doi:10.1007/s00466-019-01727-x.

[86] M. Schneider. On the Barzilai-Borwein basic scheme in FFT-based computational homogenization. *International Journal for Numerical Methods in Engineering*, 118 (8):482–494, 2019. doi:10.1002/nme.6023.

[87] M. Schneider. A review of nonlinear FFT-based computational homogenization methods. *Acta Mechanica*, 232:2051–2100, 2021. doi:10.1007/s00707-021-02962-1.

[88] J. Schröder. Derivation of the localization and homogenization conditions for electro-mechanically coupled problems. *Computational Materials Science*, 46(3): 595–599, 2009. doi:10.1016/j.commatsci.2009.03.035.

[89] J. Schröder, D. Balzani, and D. Brands. Approximation of random microstructures by periodic statistically similar representative volume elements based on lineal-path functions. *Archive of Applied Mechanics*, 81(7):975–997, 2011. doi:10.1007/s00419-010-0462-3.

[90] A. Sengupta, P. Papadopoulos, and R. L. Taylor. A multiscale finite element method for modeling fully coupled thermomechanical problems in solids. *International Journal for Numerical Methods in Engineering*, 91(13):1386–1405, 2012. doi:10.1002/nme.4320.

[91] J. Shen, G. Lu, and D. Ruan. Compressive behaviour of closed-cell aluminium foams at high strain rates. *Composites Part B: Engineering*, 41(8):678–685, 2010. doi:10.1016/j.compositesb.2010.07.005.

[92] M. Smith and T. Barnwell. Exact reconstruction techniques for tree-structured subband coders. *IEEE Transactions on Acoustics, Speech, and Signal Processing*, 34(3):434–441, 1986. doi:10.1109/TASSP.1986.1164832.

[93] C. Spieler, M. Kästner, J. Goldmann, J. Brummund, and V. Ulbricht. XFEM modeling and homogenization of magnetoactive composites. *Acta Mechanica*, 224 (11):2453–2469, 2013. doi:10.1007/s00707-013-0948-5.

[94] P. M. Suquet. Local and global aspects in the mathematical theory of plasticity. In A. Sawczuck and G. Bianchi, editors, *Plasticity Today: Modelling, Methods and Applications*, pages 279–310. Springer Netherlands, Dordrecht, 1985.

[95] İ. Temizer and P. Wriggers. Homogenization in finite thermoelasticity. *Journal of the Mechanics and Physics of Solids*, 59(2):344–372, 2011. doi:10.1016/j.jmps.2010.10.004.

[96] V. P. Tran, S. Brisard, J. Guilleminot, and K. Sab. Mori-Tanaka estimates of the effective elastic properties of stress-gradient composites. *International Journal of Solids and Structures*, 146:55–68, 2018. doi:10.1016/j.ijsolstr.2018.03.020.

[97] J. Utzinger, P. Steinmann, and A. Menzel. On the simulation of cohesive fatigue effects in grain boundaries of a piezoelectric mesostructure. *International Journal of Solids and Structures*, 45(17):4687–4708, 2008. doi:10.1016/j.ijsolstr.2008.04.017.

[98] J. Utzinger, M. Bos, M. Floeck, A. Menzel, E. Kuhl, R. Renz, K. Friedrich, A. K. Schlarb, and P. Steinmann. Computational modelling of thermal impact welded PEEK/steel single lap tensile specimens. *Computational Materials Science*, 41(3): 287–296, 2008. doi:10.1016/j.commatsci.2007.04.015.

[99] M. J. Van den Bosch, P. J. G. Schreurs, and M. G. D. Geers. On the development of a 3D cohesive zone element in the presence of large deformations. *Computational Mechanics*, 42(2):171–180, 2008. doi:10.1007/s00466-007-0184-8.

[100] R. A. van Tuijl, C. Harnish, K. Matouš, J. J. C. Remmers, and M. G. D. Geers. Wavelet based reduced order models for microstructural analyses. *Computational Mechanics*, 63(3):535–554, 2019. doi:10.1007/s00466-018-1608-3.

[101] R. A. van Tuijl, J. J. C. Remmers, and M. G. D. Geers. Multi-dimensional wavelet reduction for the homogenisation of microstructures. *Computer Methods in Applied Mechanics and Engineering*, 359:112652, 2020. doi:10.1016/j.cma.2019.112652.

[102] O. V. Vasilyev and C. Bowman. Second-generation wavelet collocation method for the solution of partial differential equations. *Journal of Computational Physics*, 165:660–693, 2000. doi:10.1006/jcph.2000.6638.

[103] C. V. Verhoosel and M. A. Gutiérrez. Modelling inter- and transgranular fracture in piezoelectric polycrystals. *Engineering Fracture Mechanics*, 76(6):742–760, 2009. doi:10.1016/j.engfracmech.2008.07.004.

[104] C. V. Verhoosel, J. J. C. Remmers, and M. A. Gutiérrez. A partition of unity-based multiscale approach for modelling fracture in piezoelectric ceramics. *International Journal for Numerical Methods in Engineering*, 82(8):966–994, 2010. doi:10.1002/nme.2792.

[105] B. G. Vossen, P. J. G. Schreurs, O. Van der Sluis, and M. G. D. Geers. On the lack of rotational equilibrium in cohesive zone elements. *Computer Methods in Applied Mechanics and Engineering*, 254:146–153, 2013. doi:10.1016/j.cma.2012.10.004.

[106] J. R. Williams and K. Amaratunga. Introduction to wavelets in engineering. *International Journal for Numerical Methods in Engineering*, 37(14):2365–2388, 1994. doi:10.1002/nme.1620371403.

[107] S. Wulfinghoff. A generalized cohesive zone model and a grain boundary yield criterion for gradient plasticity derived from surface- and interface-related arguments. *International Journal of Plasticity*, 92:57–78, 2017. doi:10.1016/j.ijplas.2017.02.006.

Publication series of the Institute of Mechanics

published to date:

2010/01 Palnau, V.: Implementierung eines netzfreien Diskretisierungsverfahrens und seine Anwendung auf die Scherbandanalyse.
ISBN 978-3-921823-51-4

2010/02 Klusemann, B.: Application of homogenization methods and crystal plasticity to the modeling of heterogeneous materials of technological interest.
ISBN 978-3-921823-53-8

2011/01 Hortig, C.: Local and non-local thermomechanical modeling and finite-element simulation of high-speed cutting.
ISBN 978-3-921823-54-5

2011/02 Parvizian, F.: Modeling of microstructure evolution in aluminum alloys during hot extrusion.
ISBN 978-3-921823-56-9

2011/03 Noman, M.: Characterization and model identification for the simulation of the forming behavior of ferritic steels.
ISBN: 978-3-921823-55-2

2011/04 Kayser, T.: Characterization of microstructure in aluminum alloys based on electron backscatter diffraction.
ISBN: 978-3-921823-57-6

2011/05 Bargmann, S.: Computational modeling of material behavior on different scales based on continuum mechanics.
ISBN: 978-3-921823-58-3

2013/01 Waffenschmidt, T.: Modelling and simulation of adaptation and degradation in anisotropic biological tissues.
ISBN: 978-3-921823-61-3

2015/01 Ostwald, R.: Modelling and simulation of phase-transformations in elastoplastic polycrystals.
ISBN: 978-3-921823-66-8

2016/01 Subramanian, M.: Phenomenological modelling and simulation of ferroelectric ceramics.
ISBN: 978-3-921823-74-3

2016/02 Clausmeyer, T.: Evolution of plastic anisotropy in metals.
ISBN: 978-3-921823-76-7

2017/01 Holtermann, R.: Computational multiscale modelling of grinding processes.
ISBN: 978-3-921823-86-6

2017/02 Bartels, A.: Modelling of evolving microstructures at different scales.
ISBN: 978-3-921823-93-4

2017/03 Dusthakar Kumar Rao, D. K.: Computational modelling of single and polycrystalline ferroelectric materials.
ISBN 978-3-921823-94-1

2019/01 Buckmann, K.: Microstructure evolution in functional magnetic materials.
ISBN 978-3-947323-09-8

2019/02 Kaiser, T.: Computational modelling of non-simple and anisotropic materials.
ISBN 978-3-947323-14-2

2019/03 Heitbreder, T.: Modelling of material interfaces at different length scales.
ISBN 978-3-947323-18-0

2020/01 Berthelsen, R.: Computational homogenisation of thermomechanical problems.
ISBN 978-3-947323-19-7

2020/02 Sievers, C.: Describing the macroscopic behavior of surfaces based on atomistic models.
ISBN 978-3-947323-24-1

2022/01 Rose, L.: Optimisation based parameter identification using optical field measurements.
ISBN 978-3-947323-31-9

2023/01 Langenfeld, K.: Continuum modeling of brittle and ductile damage: theory and computational frameworks.
ISBN 978-3-947323-41-8

2023/02 Schulte, R.: Parameter identification approaches with application to different classes of materials.
ISBN 978-3-947323-45-6

2023/03 Kaiser, T.: Multiscale multiphysics material modelling.
ISBN 978-3-947323-46-3